Circulation and Stirring in the Southeast Pacific Ocean and the Scotia Sea sectors of the Antarctic Circumpolar Current

Dhruv Balwada * and Kevin G. Speer

Department of Earth, Ocean, and Atmospheric Science and Geophysical Fluid Dynamics Institute, Florida State University, Tallahassee, Florida

Joseph H. LaCasce

Department of Geosience, University of Oslo, Oslo, Norway

W. Brechner Owens

Department of Physical Oceanography, Woods Hole Oceanographic Institution, Woods Hole, Massachusetts

John Marshall and Raffaele Ferrari

Department of Earth, Atmosphere and Planetary Sciences, Massachusetts Institute of Technology, Massachusetts

**Corresponding author address:* Dhruv Balwada, Geophysical Fluid Dynamics Institute, Florida State University, 018 Keen Building, 77 Chieftan Way, Tallahassee, FL 32306-4360

E-mail: db10d@fsu.edu

ABSTRACT

The large-scale deep circulation and eddy diffusivities in the Southeast Pacific Ocean and Scotia Sea sectors between 110^oW and 45^oW of the Antarctic Circumpolar Current (ACC) are described based on a unique lagrangian dataset spanning a large sector of the Southern Ocean. The circulation and lateral stirring are estimated using subsurface RAFOS float data collected during the Diapycnal and Isopycnal Mixing Experiment in the Southern Ocean (DIMES). The mean flow, adjusted to a common 1400m depth, shows the presence of jets in the time-averaged sense with speeds of 6cm/s in the South East Pacific Ocean and upwards of 13 cm/s in the Scotia Sea. These jets appear to be locked to topography in the Scotia Sea but, aside from negotiating a seamount chain, are mostly free of local topographic constraints in the Southeast Pacific Ocean. The EKE is higher than the MKE everywhere in the sampled domain by about 50%. The absolute magnitude of the EKE increases drastically (by a factor of 2 or more) as the current crosses over the Hero Fracture Zone and Shackleton Fracture Zone into the Scotia Sea. The isopycnal stirring shows lateral and vertical variations with local eddy diffusivities as high as $2500m^2/s$ at 700m decreasing to $1500m^2/s$ at 1800m in the Southeast Pacific Ocean and higher vales in the Scotia Sea. However, when the action of jets is taken into account, the cross-ACC diffusivity reduces significantly, with values of $500m^2/s$ and $1000m^2/s$ at shallow and deep levels respectively.

1. Introduction

The global ocean circulation is often divided into a nearly horizontal, or approximately isopycnal, component, and an overturning component that is more tightly linked to diabatic processes in the interior or at the polar extremes. The polar extremes of dense water formation create water masses that spread and fill the global ocean, but this spreading depends on the topography of ocean basins. The cold deep water formed in the northern polar regions of the Atlantic Ocean, North Atlantic Deep Water (NADW), flows south in a deep western boundary current and eventually spreads along the northern flank of the ACC on its course to the Indian and Pacific Ocean basins. A fraction of NADW is injected into the ACC in layers below the Drake Passage sill depth and can be transported across the ACC in deep geostrophic boundary currents to upwell into regions of surface buoyancy loss and be transformed into Antarctic Bottom Water (AABW). The other part of the NADW that moves into the Indian and Pacific basins is transformed to Indian Ocean Deep Water (IDW) and Pacific Ocean Deep Water (PDW) via diapycnal processes (e.g. Talley (2013)).

The shallower portions of these deep water masses of the Indian and Pacific Oceans, referred to as Upper Circumpolar Deep Waters (UCDW), form layers in the Drake Passage latitude band that are above the sill depth, sill depth being a somewhat complicated construct primarily due to the Scotia Arc and the Kerguelen Plateau. In these layers, simple theory suggests that there is no mean geostrophic flow across the 500km band of the ACC (Warren (1990)). It is often argued that the dynamics in these layers is like that of the atmosphere, where the action of eddies can produce a mean residual flux that on large scales in the Southern Ocean is towards the south. To quantify the transport of this residual flux, in the absence of accurate deep velocity fields, one needs to quantify the amplitude of the isopycnal eddy stirring (eddy diffusivity) and the large scale gradient of thickness or potential vorticity (PV). Indirect estimates with box model inversions suggest a southward flux of order 10 Sv (Lumpkin and Speer (2007), Sloyan and Rintoul (2001), Garabato et al. (2014)) in deep layers.

One view of the ACC (for a recent review see Meredith et al. (2011)) is that of a large-scale, latitudinally broad mean flow, with an eastward transport of about $140Sv$. However, there are large meridional excursions in the regions where it goes over mid-ocean ridges and approaches continents. On this broad, baroclinically unstable mean flow lies a convoluted structure of jets and eddies (Sokolov and Rintoul (2009)). The merging and splitting can at any instance be acting as a barrier to mixing and at another instance strongly mix fluid parcels. This is in marked contrast to the Gulf Stream, for example, where a single primary jet exists. The ACC jets can be locked to topography, and nearly stationary, or more freely evolving typically in regions with less topographic control (Sallée et al. (2008a)).

Although the importance of the Antarctic Circumpolar Current (ACC) to the adiabatic closure of the meridional overturning circulation has been inferred for some time, direct measurements of the strength and nature of this process have been lacking (Marshall and Speer (2012)). Here we analyze results from an observational campaign, Diapycnal and Isopycnal Mixing Experiment in the Southern Ocean (DIMES), which was undertaken in 2009-2014 to quantify the magnitude of isopycnal eddy diffusivities and diapycnal mixing. We present results from the deployment of RAFOS floats (subsurface drifters tracked by a moored acoustic network) in the South East Pacific Ocean and Scotia Sea sectors of the ACC.

2. Overview of the DIMES RAFOS float experiment

RAFOS floats were deployed as part of the DIMES experiment, primarily between the synoptically observed positions of the Sub-Antarctic Front (SAF) and Polar Front (PF) at 105^oW.

Additional floats were deployed downstream of this deployment site to supplement the dataset. The total number of floats deployed was 210. However, after failures, 140 float tracks comprising 183 years of float data (66795 float-days) were retrieved. Figure 1 shows summary of the experimental design and regional geography, together with the mean SSH contour lines that envelope the extent of the initial float deployment relative to the ACC and the climatological position of the SAF and PF according to Orsi et al. (1995). The SSH and frontal positions mark the southward drift of the ACC from its northerly excursion along the Pacific-Antarctic Ridge, crossing it through two major fracture zones near latitude $55^o S$, the apparent contraction through Drake Passage, to enter the Scotia Sea and finally exit north over the North Scotia Ridge. The frontal positions also show the large scale meandering of the PF and to as lesser extent the SAF. The float trajectories are divided into shallow and deep floats based on their mean depth being greater than or smaller than 1400m and qualitatively show a very similar behavior (Figure 2). These trajectories also clearly show complexity created by the meso-scale eddies and presence of vertical shear, the latter apparent from the longer displacements of the shallower floats.

Although many floats were deployed north of the historical position of the SAF all floats proceeded east and exited the Southeast Pacific Ocean; remarkably, none moved northward sufficiently to be trapped and subsequently circulate in the subtropical gyre of the Pacific Ocean. This behavior is in agreement with Faure and Speer (2012), who show the presence of a mean flow toward the ACC in the interior layers between 1000-3000 m. In contrast, on the southern side of the ACC, a few floats did appear to be continuing to move south, away from the core of the ACC.

The duration of the experiment was from 2009 to 2011 with the highest number of float-days (one float tracked for one day) sampled in 2010 (Figure 3). The floats were ballasted to stay near two isopycnal surfaces of neutral density 27.6 and 27.9 σ. However due to technical failures the behavior was closer to that of isobaric floats. The distribution of float days in depth shows a bimodal structure with peaks at 800m and 1400m corresponding to the mean positions of the ballasting isopycnals. As the floats did not maintain their target density, the float-days distribution in temperature is wider showing only a single peak. A distribution of float days over topographic depth following the float shows a peak at 4500m corresponding to the mean depth of the Southeast Pacific Ocean. This distribution also has a long tail towards shallower depths corresponding to the passage through the Scotia Sea, where topographic variability is greater and topographic features often reach within a few hundred meters of the surface.

The concentration of floats, or density in float-days, is highest near and just downstream of the deployment site at 105^oW; a secondary peak is seen near the downstream deployment at 75^oW (Figure 4a). These figures show the probability, given by the number of float-days in a bin divided by the total number of float-days, that a float or passive tracer will pass through a bin if a tracer source was present at the float deployment location (Ollitrault and Colin de Verdière (2002)). This provides a complementary view of the flow kinematics in the region compared to the one provided by the tracer release experiment (Tulloch et al. (2014)). The concentrating effect of the convergence of the ACC into Drake Passage is apparent.

Another representation of the float density is provided (Figure 4b). Here, the number of floats passing through each longitudinal section is summed in meridional bins and then normalized by the total number of floats that pass through that longitudinal section. This effectively renormalizes the concentration as the float cluster evolves downstream. Details of the local, transient, transport pathways in the broader eastward flow are revealed more clearly, with the SAF and PF distinct from about 95^oW to 75^oW, followed by convergence, then separation again along the northern boundary and topographic ridges in the Scotia Sea. Comparison with f/H (Figure 4b) shows a tendency to conserve large-scale potential vorticity up to about 75^oW.

A qualitative sense of the ACC flow and its prominent features during the experiment emerges from the tracks and the geographically binned (eulerian) displays. One of these is a large meander at $100^o W, 59^o S$, which was experienced by the floats in both the 2009 and 2010 deployments. Hovmoeller plots of SSH show that this is not a permanent flow structure, but nevertheless does show a tendency to reappear in this region. This meander splits into two jets at $95^o W$ presumably upon interacting with the San Martin Seamounts. We speculate that one of these jets is associated with the PF and the other with the SAF. The jets merge as they approach Drake Passage, move northward and make their way over the northern ends of the Hero Fracture Zone and the Shackleton Fracture Zone through deep troughs, into the Yaghan Basin. Once in the Yaghan Basin, the floats are again divided into two groups following topographic contours of of the continental slope on the northern side and the West Scotia Ridge on the southern side of the Yaghan Basin. They exit the Scotia Sea through the openings in the North Scotia Ridge beyond which tracking becomes problematic as the topography blocks most of the sound source signals.

We focus here on velocity statistics and isopycnal mixing derived from the RAFOS float observations. A companion paper provides greater descriptive detail of the lagrangian aspects of the observations (Balwada et al. (2015), to be submitted). Along with the float data, sea-surface height (SSH) estimates were also used in this study for an approximate streamfunction and for surface geostrophic velocities. These data were obtained as absolute dynamic topography (ADT) data, an altimeter product produced by Ssalto/Duacs and distributed by AVISO, with support from CNES (http:/www.aviso.altimetry.fr/duacs/).

3. Eulerian Mean Flow

a. Vertical structure

Float velocities are first compared to the available velocity fields from SSH and then averaged in vertical bins to get the structure of the absolute velocity as a function of depth. It is important to note that this comparison of float velocities to SSH velocities should not be expected to be highly accurate due to resolution limitations of the AVISO altimeter.

The SSH fields are available in 7 day averaged fields, which are then used to calculate the surface geostrophic velocities ($\psi = \eta/(f\rho_o)$). The float velocities, resolved daily, are smoothed using a 3 day running mean to compare against SSH derived fields. We calculate the ratio of the float speed to the SSH derived speed and the angle between the two velocities. These are then binned in depth bins for each of the basins (Southeast Pacific Ocean and Scotia Sea) and plotted in Figure 5. The e-folding scale of the mode of the ratio is approximately 1650m in the Southeast Pacific Ocean and 1300m in the Scotia Sea, however it is important to note that this fitting can have large errors due to the large standard deviations of the ratio in each bin. This large standard deviation is a result of both the time variability of the current and also the variation in decay scale (decreasing to the south, Karsten and Marshall (2002)) as the mean stratification changes across the ACC. The probability distribution function (PDF) of angle between surface and float velocities vs depth has a mean of zero and a standard deviation around $50^o - 55^o$ for almost all bins with slightly higher values for the deepest bin in the Southeast Pacific Ocean.

The ACC is often assumed to have an equivalent barotropic (EB) structure (LaCasce and Isachsen (2010)), which was suggested based on FRAM model output by Killworth (1992) and further discussed dynamically by Hughes and Killworth (1995). They showed that an EB solution can be derived based on geostrophic dynamics assuming a f-plane with small vertical velocities. Observations (Phillips and Bindoff (2014)) have shown some broad consistency with the model, showing vertical coherence and small turning of velocity vectors with depth. However, the observations also show that this model breaks down in regions of strong cross topographic flows, where large vertical velocities would be present. It is also important to note that this model must break down to allow cross ACC flows and the presence of the upper limb of the meridional overturning circulation. Hughes and Killworth (1995) showed that

$$\theta_z = -\frac{N^2 w}{f|u|^2} \tag{1}$$

where N^2 is the usual Brunt-Vaisala frequency, w is the vertical velocity, f is the coriolis force, $|u|$ is the flow speed and θ_z is the change of angle between the flow at two vertical positions with depth. In what follows we use these relations to describe the observed patterns. The above mentioned result, as noted by Hughes and Killworth (1995), is equivalent to Stommel's β spiral.

Ratios and angles between the float and SSH derived velocities are binned as a function of surface speed (Figure 6). Firstly, the ratio of the float speed to the surface speed is more variable for slower speeds and also more variable for similar speeds in the Scotia Sea when compared to the Southeast Pacific Ocean. Secondly, the variability of the angle between the SSH derived velocity and float velocity is greater for slower speeds and also this variability is slightly greater in the Scotia Sea compared to Southeast Pacific Ocean for the same speeds. The positions of the floats corresponding to slower surface speeds are not necessarily located on the boundaries of the ACC or over rougher topography where the EB assumption might break down, but rather spread throughout the region, similar to the float positions that correspond to the other speed bins. We can explain these results, at least qualitatively, using the above mentioned relation (equation 1). Based on this relation weaker surface speeds imply a greater turning with depth, for a given w, as turning with depth is inversely proportional to the square of the surface speed. Also based on this relation there should be greater turning if there are stronger vertical velocities, for a given speed, as there will be in the Scotia Sea due to rougher topography. Hughes (2005) has shown that in the ACC the vertical velocities generated by topography are an order or magnitude higher than the vertical velocities that are generated by wind stress. It still remains unclear as to why slower surface speeds lead to a greater mean ratio and variability of the ratio between float speed to surface speed.

Vertical structure of basin averaged velocities and their variances (Figure 7) were computed using the raw velocities with no filtering, in contrast to what was done previously to compare to SSH. The mean zonal velocity decreases from a value of 6cm/s at 600m to close to 1cm/s at 2400m in the Southeast Pacific Ocean. The mean meridional velocity is close to zero ($< 1cm/s$) with a slight southward flow component (associated with the southeastward ACC flow). The velocity variance in the Southeast Pacific Ocean also shows a decrease with depth, dropping from a value of $80cm^2/s^2$ to $20cm^2/s^2$. The zonal and meridional variances have a similar structure in the vertical. They decreases rapidly up to 1300m and at greater depths they decrease more gradually, implying a reduction in vertical shear with depth. The Scotia Sea has a velocity profile that shows higher magnitudes of mean speed and velocity variance than the Southeast Pacific Ocean sector and also decreases with depth. The mean zonal velocity decreases from 10cm/s at 400m to 5cm/s at 1800m. The mean meridional velocity is positive as the ACC flows north with velocities of 7cm/s near 400m decreasing to 1cm/s at 1800m. The variances are similar in the zonal and meridional directions, from $250cm^2/s^2$ at 400m to $60cm^2/s^2$ at 1800m. The decay is again rapid up to 1300m and thereafter more gradual.

b. Horizontal Structure of flow

The mean flow was estimated by binning the float velocities into 2.0^o zonal by 0.5^o meridional bins. This choice was made based on the knowledge that the flow structures are usually zonally aligned with meridional variability. The size of the bins was chosen such that the bins were large enough to encompass sufficient number of data samples but also small enough to resolve the flow structures that are present in the mean flow. It is important to recognize that the variability or EKE measurements in each bin reflect not only the time variable component but also the mean horizontal shear that might be present in the region covered by the bin. As the floats were spread unevenly in the vertical in each bin, an adjustment/rescaling was done to the horizontal velocities to approximate the corresponding velocity at the 1400m depth level (this is level where the highest number of float days were sampled). This adjustment was done assuming an EB structure and using the mean speed vertical profile in each of the basins, calculated using all the float velocities (separately for the Southeast Pacific Ocean and Scotia Sea). Adopting this rescaling approach to ensure more statistical reliability seems acceptable based on the results shown in the previous subsection. We also checked to see if the residual velocities were gaussian by performing a Kolmogrov-Smirnov statistical test, and found this to be approximately true with p values around 0.3 in the Southeast Pacific Ocean and 0.9 in Scotia Sea as shown in Figure 8.

To clarify the relation between the averaged data and the underlying trajectories we also present selected trajectory segments, chosen as follows. The float tracks were subdivided into 120 day segments and then for each segment the ratio (ε) of float displacement to the total distance was calculated

$$\varepsilon = \frac{\int_0^{120} \bar{U} dt}{\int_0^{120} \bar{u} dt} = \frac{\int_0^{120} \bar{U} dt}{\int_0^{120} \bar{U} dt + \int_0^{120} \bar{u}' dt} \tag{2}$$

This ratio is always less than 1, more so when the integrated residual velocity (or looping) component is larger. This ratio was used to group the tracks into looping and other, non-looping segments.

In the Southeast Pacific Ocean there are three primary regions where looping is found (Figure 9). The first one is a single large eddy near the deployment line ($105^o W$) in which many floats were deployed. The second location is both upstream and downstream of the San Martin Sea Mounts. The upstream location is associated with the crest of the large meander where the flow appears to split into smaller eddies and the downstream location is associated with larger loops. The third region of looping is found around 85^oW and 60^oS. The straighter float tracks lie in regions of time mean jets, as seen in eulerian means discussed below, which are located on the northern and southern sides of the looping regions. In the Scotia Sea the strong recirculation of the Yaghan Basin stands out (Figure 11). There is another looping area where the EKE increases for the second time downstream of the Yaghan Basin. The straighter trajectories appear to trace out the continental slope and West Scotia Ridge, similar to the strong mean flows discussed below.

The binned mean velocity field in Southeast Pacific Ocean (Figure 10) shows primarily an eastward zonal flow in two principal jets spaced approximately 200km apart, with a small southward component. The maximum bin averaged speeds at 1400m are approximately 6-8cm/s in the core of the jets. We identified these jets as the SAF and PF based on the hydrographic properties associated with strong flows that were observed during the deployment cruises (not shown). The PF shows a meander in the binned mean flow upstream of the San-Martin seamounts at 95^oW, 59^oS, which seems to be associated with the barotropic PV (f/H). This is probably the reason for the repeated appearance of the large meander at this location, as was seen in Hovmoeller plots and by the two float deployments. The San Martin seamounts at 95^oW, 59^oS are associated with a weaker mean flow, which extends somewhat downstream of the seamounts.

The meandering of the jets, upstream of the San Martin seamounts, is associated with a slightly higher EKE. The northern jet flows along f/H contours near 57^oS and 90^oW, and weakens downstream where the f/H contours diverge. This divergence of f/H contours is collocated with a tongue of high EKE signal - the highest in the Southeast Pacific Ocean - which is also one of the regions where large looping is seen. The standard deviation ellipses in this region are primarily isotropic, with a slightly greater zonal component associated with the region where the highest EKE is observed in the region.

In the Scotia Sea (Figure 12), the strongest average speeds near the 1400m level are 14-16cm/s, which is twice that of the Southeast Pacific Ocean. The mean velocity vectors in this region have a northward component associated with the ACC turning north and crossing over the North Scotia Ridge. The plot of speed shows the ACC approaching the Shackleton Fracture Zone as a single broad jet, with the strongest flows located near the northern side of the Drake Passage. This jet splits into two branches as it crosses the Shackleton Fracture Zone. The northern branch closely hugs the continental slope of South America, like a boundary current, and the southern branch goes south of the Yaghan Basin over the West Scotia Ridge. A strong cyclonic recirculation associated with the topographic depression in the Yaghan Basin, as the mean velocity vectors turn westwards in the center of the basin. The segments of the trajectories shown in Figure 11 also showed the presence of a recirculation in this region.

High EKE is evident downstream of the Hero Fracture zone and Shackleton Fracture zone, in the Yaghan Basin (Fig. 12). This increase in EKE is probably associated with instabilities related to crossing over the two fracture zones and the time variability of the Yaghan Basin topographic recirculation. The highest EKE signal in the Scotia Sea is found near 56^oS and 51^oW. This is downstream of the region where the two topographic jets merge and possibly interact with a topographic bump located at 54^oW and 55^oS. This region also shows significant looping in the trajectories. The standard deviation ellipses, similar to the Pacific Ocean sector, do not have a strong preferred orientation except in some bins near the boundaries, where they are oriented along the topography.

c. Vertical motion of floats

The spatial variability of the high frequency vertical motions of the floats was calculated by taking a 3 day running mean of the pressure time series from each float and removing this component from the original time series in order to calculate a high frequency residual time series. This residual is the high frequency component of the pressure signal or δ pressure. It is clear in individual float trajectory time series that the high frequency pressure variation increase significantly as the float goes through the Drake Passage and enters the Scotia Sea (Balwada et al. (2015)).

The rate of change of the high frequency component may be calculated, giving an (aliased) view of the vertical motions of the floats due to short time-scale processes. It may also be interpreted as a measure of the maximum amplitude of vertical motions due to small scale processes. Similar to the previous sections, we first separate these data into a Southeast Pacific Ocean and Scotia Sea areas and calculate the vertical profiles of the vertical motions in depth bins (Figure 13a). The binned mean of the vertical motion was zero as would be expected for high frequency components (not shown). The variance decreases with depth and is significantly higher in the Scotia Sea compared to the Southeast Pacific Ocean.

Vertical profiles of the pressure variance were used to rescale the rate of change of the vertical motions from all depth levels to a common level of 1400m. These rescaled vertical motions were then binned in geographical bins ($2^o \times 1^o$) and the variances and means calculated for each bin. The means were approximately zero with no significant spatial pattern. The variance (Figure 13b), similar to the mean speeds and EKE presented in the previous sections, increase significantly in the Scotia Sea. The highest variances, almost 2 orders of magnitude higher than the Southeast Pacific Ocean, were observed along the continental slope and along the North Scotia Ridge in the

Scotia Sea. This increase is consistent with a greater lee wave activity in the Scotia Sea, associated with strong flow over ridges.

4. Length scales, time scales and isopycnal stirring

For the analysis that follows we divided the region into six groups as defined next, unless otherwise noted. Three divisions in the zonal direction ($110^oW - 90^oW$, $90^oW - 70^oW$ and $70^oW - 30^oW$) and two divisions in depth (500 - 1400 m and 1400 - 2500 m). For each division, the mean ($U_i =< u_i >= 1/N \sum u$), where the sum is over all available observations and N is the number of observations, and residual ($u'_i = u_i - U_i$) velocities were calculated. Subscripts i or j represent the direction (zonal, meridional). The means and the corresponding variances are presented in Table 1. The errors were calculated using standard error calculation methods, similar to the ones described by Ollitrault and Colin de Verdière (2002). The Reynold's fluxes (not shown) were calculated and are negligible for such large area averages.

Spatial correlations are calculated as

$$C^e_{ij}(r) = \frac{(< u'_i(x) u'_j(\vec{x}+r) >)}{< u'_i(\vec{x}) u'_j(\vec{x}) >} \tag{3}$$

where r is the separation between the floats and the averaging is done in 50 km r bins using samples at all times. This correlation is then used to calculate the eulerian integral length scale.

$$L^e_{ij} = \int_0^\infty C^e_{ij}(r) dr \tag{4}$$

This calculation is done using two methods as described below because we cannot integrate observational correlations to infinity. 1000 noisy correlation curves are generated using the mean correlation curve plus gaussian noise within two standard errors. In the first method these noisy correlation curves are integrated out to the first zero crossing. In the second method an exponentially decaying function is fit to the noisy correlation curves and the decay scale is given by the fitting. Both methods produce 1000 estimates, corresponding to each noisy correlation curve that was generated. The average of these estimates is taken to be the length scale and the error is represented as one standard deviation of these estimates. The results are shown in Table 1. Both procedures produce very similar length scales with the exception of the deep Scotia Sea, where observations are scarce.

The spatial correlation function (C^e_{ij}) was calculated as well (not shown). It has a structure that is commonly seen, decreasing exponentially followed by a negative lobe and then oscillation around zero until it decays completely. We interpret the negative lobe as a signature of cyclonic and anticyclonic eddies that are present in an alternating patterns, as is often seen in experiments (Sommeria et al. (1989)) and other regions of the ocean such as the Gulf Stream. The length scale is approximately 60km for most of the region, with slightly larger scales in the west at the shallower level. We interpret the greater scales in the west as an imprint of the large meander that was seen by many of the floats (Balwada et al. (2015)).

We also present the distance at which the first and second zero crossing occur for the correlation function (Table 1). This gives a sense of the distance at which the velocities broadly reverse, or the diameter of the eddies. This scale is approximately 130 km for most of the region, which is in broad agreement with the eddy sizes calculated for this region using SSH fields (Chelton et al. (2011)).

To inspect the properties in frequency domain we divided the trajectories into 120 day segments. Each segment was assigned its corresponding spatial bin based on its mean position and mean depth. The binned time series are then used to calculate the lagrangian frequency spectra $S(\omega)$ of the velocity time series. This is presented in variance preserving form (Figure 14). The lagrangian frequency spectra show a broad peak that migrates to high frequencies as the floats moves east, and is also located at higher frequencies in the same geographical bin at the shallower depth. The peak migrates from periods of approximately 60 days in the deep western part of the Southeast Pacific Ocean to periods of 15 days in the shallow Scotia Sea. This can be explained as a consequence of Doppler spectral shifting that can occur in the presence of mean flow as discussed in Chen et al. (2015).

The lagrangian spectra were also plotted on a log-log axis (not shown) to determine spectral slopes. The spectra at periods smaller than 7 days have slopes steeper than -3, which implies that motions at these time scales are not contributing to the lagrangian dispersion. The spectra at periods between approximately 7 and 60 days have spectral slopes between -3 and -2. The spectra flatten at periods larger than 60 days (lower frequencies), which is a critical requirement for the eddy diffusivities to exist. If the spectra do not flatten at low frequencies the power of the spectra at zero frequency does not necessarily converge, implying that the the diffusivity is undefined (Rupolo et al. (1996)).

The binned time series are also used to calculate the velocity autocorrelation.

$$R^l_{ij}(\tau) = \frac{< u'_i(t)u'_j(t+\tau) >}{(< u'_i(t)u'_j(t) >)} \tag{5}$$

The angular brackets represent averaging over the trajectories that are present in the bin. This correlation is then used to find the lagrangian integral time scale.

$$T^l_{ij} = \int_0^\infty R^l_{ij}(\tau)d\tau \tag{6}$$

Structurally, R^l_{ij} looks similar to C^e_{ij}: there is a decay and oscillations, usually with a prominent negative lobe. This structure would be expected based on a turbulent field in which the flow decorrelates in time but also has the presence of significant looping and meandering. This can be approximated as a function of the form:

$$R^l_{ij}(t) = e^{-t/T_{eij}} cos(2\pi t/4T_{dij}) \tag{7}$$

where T_{eij} is a decay scale and T_{dij} is the time of first zero crossing or the meander time scale. This form is fit to the mean autocorrelation functions; the parameters and error in fits is calculated using bootstrapping. This is done using the method of producing noisy correlation functions as described above, used for spatial correlation integration. Previous observational studies using lagrangian measurements (Sallée et al. (2008b), Garraffo et al. (2001)) have fit a functional form of the type shown above or similar forms.

Klocker et al. (2012) applied the mixing suppression theory (Ferrari and Nikurashin (2010)) to particles instead of tracers and derived an autocorrelation function of the same form as (7). This links physical processes to the presence of the two scales using dynamical arguments. Their theory was derived for a randomly forced Rossby wave solution to a quasi-geostrophic system. The non-linear terms, used as forcing for the Rossby waves, were parameterized as a sum of a white noise process and linear damping. The decay time scale (T_{eij}) was associated with the the linear damping time scale. The oscillation time scale (T_{dij}) was based on the dominant wave number multiplied by the difference of mean speed and observed phase speed. This difference is associated with the mean PV gradient based on the dispersion relation for linear Rossby waves. Their expression for the autocorrelation is (their eqn 18)

$$R_{vv}(t') = \frac{2k^2 EKE}{K^2} e^{-\gamma t'} cos[k(c_w - U)t'] \tag{8}$$

where k is the zonal wave number, K is the amplitude of the total wave number, γ is the linear damping constant, c_w is the observed phase speed and U is the mean zonal speed. Based on this model, a stronger PV gradient (larger $|c_w - U|$), holding the damping time scale constant, would call for the the oscillation time scale to be relatively smaller. This would, in turn, imply a more prominent negative lobe in the autocorrelation function. A larger negative lobe implies a smaller lagrangian integral time scale and smaller eddy diffusivities.

Based on eqn (8) we can calculate a theoretical meander time scale using the binned mean flow, observed feature propagation speeds(c_{wi}) from Fu (2009) and observed length scales.

$$2T_{dii}^{theory} = \pi/(k_j.(c_{wj} - U_j)) \tag{9}$$

The analytical integral of this chosen autocorrelation function gives an effective lagrangian integral time scale

$$T_{ij}^{l} = \frac{4T_{eij}T_{dij}^2}{\pi^2 T_{eij}^2 + 4T_{dij}^2} \tag{10}$$

These time scales are presented in Table 1. The integral time scale (T_{ij}^{l}) approaches the decay time scale (T_{eij}) as the meander time scale (T_{dij}) gets relatively longer. This happens when the meander time scale is long since the amplitude of the autocorrelation function will decay to a very small value before the negative lobe can significantly affect the integral. This leads to the fitted T_{duu} being very large ($>$ 500days) for most of the bins and those results are not shown in the Table.

The decay time scale, which generally increases with depth, is about 10 days in the Southeast Pacific Ocean and 6 days in the Scotia Sea. This is expected based on simple scaling arguments so that $T_{eij}^2 \propto \frac{1}{|k|^2 u_{ij}'^2}$ and the fact that the length scales are similar at the shallower and deeper levels. This is different than the result in Lumpkin et al. (2002); they found that the time scale remained roughly constant with depth and the length scale decayed with depth in the North Atlantic Ocean. The eulerian time scale calculated using current meters in different parts of the ACC are close to 20 days. Phillips and Rintoul (2000) presented these numbers for a mooring array south of Australia and compared it to the time scales calculated in the Drake Passage during FDRAKE. It is not surprising that the eulerian timescales are larger than the lagrangian time scale, as the floats propagate through eulerian features faster than the eulerian features pass through a region (Middleton (1985-02-01T00:00:00)).

We then use these time scales and EKE to calculate the eddy diffusivities ($\kappa_{ij} = EKE.T^l_{ij}$). The meridional diffusivities are similar in the two Southeast Pacific Ocean bins; approximately $2200m^2/s$ in the shallower bins and $1400m^2/s$ in the deeper bins. The meridional diffusivity is approximately $3200m^2/s$ in the Scotia Sea. The zonal diffusivities are generally greater, and this is to be expected because they are enhanced by both the mean horizontal shear and mean vertical shear, which cannot be completely removed by removing a bin averaged mean to find the residual velocities. In the Scotia Sea both the zonal and meridional diffusivities seem to be affected by these shears.

Using the results from the above analysis, that the scales are similar across the Southeast Pacific Ocean, we use all the tracks between $110^oW - 70^oW$ and increase the number of vertical bins to resolve better the vertical structure of diffusivity. The diffusivity is calculated the same way as above by first fitting to the autocorrelation function and calculating the time scales. The diffusivity calculated using only the decay time scale ($K_o = EKE.T_{eij}$), the diffusivity calculated using the lagrangian integral time scale called the suppressed or expected diffusivity ($K = EKE.T^l_{ij}$) and the theoretical estimate of diffusivity ($K^{theory} = \frac{4EKET_{eij}T^{theory2}_{dij}}{\pi^2 T^2_{eij} + 4T^{theory2}_{dij}}$) from Klocker et al. (2012) are shown together in Figure 15. The presence of mean flow or the presence of a negative lobe in the auto-correlation function suppresses diffusivity, which is evident as K_o is greater than K everywhere. In the calculation of K^{theory} the observed decay time scale is used as there is no other way to calculate it. T^{theory}_{dii} for this figure was calculated using a length scale of 100 km as it provided a better fit against the observed diffusivity than using the calculated length scale from spatial autocorrelations. This value is higher than the calculated integral length scales (60 km) but smaller than the length scale of the first zero crossing (100 km). Thus, the theoretical value should be regarded as a fitted form rather than an absolute prediction.

It has been pointed out that in the ACC, diffusivities can take 6 months or longer to asymptote to a constant value LaCasce et al. (2014), if the diffusivity is calculated as $< X^2 > /2T$ or some similar measure (LaCasce (2008)). If this holds, calculating binned diffusivities is problematic, as the floats spend only a fraction of 6 months in a bin. Another reason binned diffusivities were not calculated in this section is because the floats are spread in the vertical; for the mean flow calculations we could use the EB assumption to rescale the float velocities to a common depth level but no similar procedure can be applied to rescale the float trajectory to a common depth level. What we have presented in this section are in essence binned diffusivities, but with the choice of the bin size being very large ($30^o lon \times 10^o lat$) much larger than the bins for the mean flow. Previous float and drifter studies have presented diffusivities in bins the same size as the bins used for describing the mean flow (e.g. Ollitrault and Colin de Verdière (2002), Swenson and Niiler (1996)), but using a dataset that was primarily limited to a certain depth level or the sea-surface.

Keeping these facts in mind, the dispersion is calculated for the Southeast Pacific Ocean and the Scotia Sea float tracks divided into two depth bins, in cross-SSH coordinates (Figure 16). The diffusivity is estimated as $< X^2 > /2T$, where X is the cross stream distance. The diffusivity estimates, using this calculation, are approximately $500 m^2/s$ and $1100 m^2/s$ for the shallow (500-1400m) and deep (1400-2500m) Southeast Pacific Ocean floats. In the Scotia Sea the diffusivities are approximately $1200 m^2/s$ for the both shallow (500-1000m) and deep floats (1000-2000m) but with larger error bars. These limits of the depth bins were chosen to allow for an almost equal data distribution in both depth bins. The division between Southeast Pacific Ocean and Scotia Sea was chosen to be $70^o W$. The error bars on the dispersion are calculated using bootstrapping where the trajectories are resampled allowing for repeats and the dispersion curves calculated a 1000 times. The error in the dispersion figure is calculated as one standard deviation of the bootstrap samples. For the diffusivity curve the error is the range of slopes that fit between the errorbars of the dispersion curves. In the Southeast Pacific Ocean there are about 55 floats for each depth bin at the first day and this number only marginally decreases to about 45 by day 250. However in the Scotia Sea, on there first day, there are about 40 floats but within 150 days this number decreases to around 15. The choice of coordinates does not affect the diffusivity estimate in the Southeast Pacific Ocean as the SSH contours are almost zonal (Tulloch et al. (2014)).

In the Scotia Sea use of the across SSH dispersion allows the quantification of cross streamline mixing, which cannot be done by calculating zonal and meridional diffusivities. Similar to LaCasce et al. (2014), the shallower diffusivities decrease over time and end up smaller than the deeper diffusivities in the Southeast Pacific Ocean after 150 days. It is not quite clear what sets this 150 day time scale, considering the decay scale is about 10 days. The dispersion of the shallow floats in the Southeast Pacific Ocean does not grow linearly but saturates after some initial increase, whereas the dispersion from the deeper floats in the Southeast Pacific Ocean increases almost linearly as would be expected for a diffusive process.

Is there a mid-depth maxima in diffusivity, and if so then why does it exist? To answer this question we compared the different estimates of diffusivity for the Southeast Pacific Ocean. LaCasce et al. (2014) presented a single vertically averaged isopycnal diffusivity from the same float data as here and Tulloch et al. (2014)) gave a measure of diffusivity at the tracer isopycnal level using the tracer surveys. These studies also presented a vertical structure of diffusivity that was calculated by releasing particles and tracers in a model and advecting them using the model velocity field. Their modeling results showed that the vertical structure of diffusivity had a mid-depth maxima of about $1000m^2/s$ at approximately 2000m and it was reasoned that this was a result of mixing length suppression at shallower depths in the presence of stronger large-scale mean flow. However, it took longer than 6 months to asymptote to this value using the particles, and a long term (100-500 days) linear fitting was done to the second moment of the tracer concentrations. In contrast, Bates et al. (2014) presented an area averaged diffusivity from SSH observations and ECCO output and did not obtain a mid-depth maxima in diffusivity. Bates et al. (2014) results were based on using a length scale that was calculated from SSH fields (Chelton et al. (2011)), assuming it to be the dominant length scale. Recently, Chen et al. (2015) provide diffusivities in the DIMES regions using an approach that accounts for contributions of multiple length scales by integrating over the wavenumber-frequency spectra in the region. Interestingly, their spatial maps of eddy diffusivities show a significant degree of inhomogeneity. To calculate a single vertical profile of eddy diffusivity over the region they do a simple area averaging, similar to the Bates et al. (2014) work. They obtain some hints of a mid-depth maxima in their results but generally the trend of eddy diffusivity is to decrease with depth.

Naveira Garabato et al. (2011) calculated mixing lengths in the ACC using hydrographic data and showed the presence of suppressed mixing lengths in frontal regions of the ACC, at least in regions of smooth topography and essentially zonal jets. Naveira Garabato et al. (2011) applied the mixing suppression ideas in a more local sense, by calculating the mixing length as the RMS temperature fluctuation divided by the large scale temperature gradient on neutral surfaces. In summary, the results above can be divided into three categories: local estimates (Naveira Garabato et al. (2011)), eulerian estimates that are spatially averaged (Bates et al. (2014), Chen et al. (2015)) and longer term estimates using lagrangian passive tracers (LaCasce et al. (2014), Tulloch et al. (2014)).

It is important to remember that the ACC is a region of a complex flow bands of low EKE and negligible mean flows along with strong mean flows or jets. The regions within the ACC where the mean flow is weaker, such as between localized jets, could have large diffusivities and be well-mixed regions, while the regions of strong jets act as barriers to cross-stream mixing. However, if the jets merge and split they might not always be barriers to mixing. Probably because the Southeast Pacific Ocean is a relatively simple region, the jets persist for long durations without much splitting and merging and act as barriers (Thompson (2010)). This hypothesis for the Southeast Pacific Ocean is supported by our binned mean flow estimates showing jet like structures and also the results of Thompson et al. (2010), who showed that the region between the Udintsev Fracture Zone and the Drake Passage had the most number of distinct PV pools or regions of homogenized PV, compared to any other region of the Southern Ocean, implying that strongly mixed regions exist in the Southeast Pacific Ocean but there is little mixing between each of them.

We believe that the discrepancy between the various eulerian estimates, which are similar to our initial estimates using a functional fit to Lagrangian autocorrelation function (Figure 15), and longterm lagrangian passive tracer estimates, which are similar to our second estimate using long term dispersion calculations (Figure 16), arises because of the nature of the averaging used to estimate a single number for diffusivity over a large region. The correct way to average diffusivities in a cross stream direction was shown in Nakamura (2008) for the atmospheric case. Using a 1D, zonally averaged model the correct predictor of eddy diffusivities was shown to be the harmonic average ($K_{average} = (\int 1/K(y)dy)^{-1}$), where regions of low mixing dominate the average. This model holds if the region has barriers that are invariant in time; a zonally uniform flow (along stream) might be a good assumption for the Southeast Pacific Ocean as discussed earlier. Hence, a lagrangian passive tracer spreads through a region and converges to the harmonic mean rather than an area average, as was made in the eulerian estimates. However, it remains unclear as to what is the proper averaging methodology if the regions is not zonally homogeneous and the barriers merge and split in space and time, which would better represent the ACC.

Overall, our results appear to be consistent with these previous notions and results. Jets are faster at shallower levels and act as stronger barriers to mixing, while at deeper levels the jets slow down and the barrier effect becomes weaker. Also, the regions between the jets at shallow levels are more strongly mixed than at deeper levels simply because of the higher EKE at shallower levels. To confirm this, the model particle calculations of LaCasce et al. (2014) were revisited (not shown here). Calculations of dispersion at shallower levels showed saturation after an initial growth period of about 50-100 days, similar to the saturation seen in Figure 16. Long integrations, longer than about 6 months, produced lower diffusivities similar to the diffusivity calculations above using dispersion in the cross stream direction.

5. Discussion

The DIMES floats provide a striking set of trajectories that quite clearly show both the large-scale circulation and the turbulent nature of the flow in the ACC. The floats sampled depths between 500 and 2500 m from 105^oW to 40^oW, primarily between the SAF and PF. At a depth level of approximately 1400m in the Southeast Pacific Ocean the mean speeds ranged from 6 cm/s in the jets to 1cm/s between the jets, whereas in the Scotia Sea the typical speeds were almost doubled. The EKE in the two regions also differed substantially, $10-60cm^2/s^s$ in the Southeast Pacific Ocean, and $20-140cm^2/s^2$ in the Scotia Sea, at similar depths. The EKE and the mean speeds increase as the flow crosses over the Hero Fracture Zone and Shackleton Fracture Zone, from the relatively calm Southeast Pacific Ocean to the vigorously unstable Scotia Sea. The flow at various depths shows good semblance to the flow at the surface observed by satellites and leads us to believe that the flow is EB to first order. The vertical motions of the floats, dominated by shorter time scale phenomena, also show an order of magnitude increase from the Southeast Pacific Ocean to the Scotia Sea and are the highest over the continental slope of South America.

No previous direct measurements of large-scale mean flow and variability exist in the deep Southeast Pacific Ocean against which we can compare results. However, current meter measurements from different sites in the ACC, primarily south of Australia and in the Drake Passage region, found similar flow statistics (Phillips and Rintoul (2000), Ferrari et al. (2012), Firing et al. (2011)). Phillips and Rintoul (2000) compared the vertical structure of the flow with older current meter measurements from the FDRAKE experiment and their results are qualitative similar to ours. The mean vertical shear generally decreases with depth, in agreement with our results. The velocities from the current meter in other regions also show a correspondence with the SSH derived velocity fields that generally decreases with depth. Our results show congruence with the SSH derived velocities but no significant change with depth, as we do not see any evidence of greater turning in deeper versus shallower bins. Instead, we notice that the relationship is weaker with a decrease in surface speed, perhaps due to sampling considerations with the altimetry.

The jets observed in the mean flow estimate of the Southeast Pacific Ocean and Scotia Sea have scales and separations that are very similar to the eddy length scales in the region. They also show meanders at scales similar to the eddy scale, set by the meanders in the Southeast Pacific Ocean and also set by the scale of the topography, especially in the Scotia Sea. It is important to realize that these structures exist over time scales that are longer than time scale of passage for the particles through the region, which is the reason they are seen in the mean field, and could be significantly affecting the spreading of tracers. We speculate that the spacing between the jets in Southeast Pacific Ocean basin is initially set upstream by the spacing between the fracture zones in the Pacific-Antarctic Ridge. Subsequently, the approximately 200km spacing seen in this region is probably set by a combination the weak non-uniformities in f/H gradients and upstream effect of the seamounts. The extent to which a Rhines' scale-like separation between the jets plays a role, as can be expected in a nearly flat bottom ocean basin, is difficult to evaluate. It is important to remember that the topographic features will play a role in setting the circulation at mid-depth if the velocities along the bottom are non-trivial, which (for depths greater than 2500m) is a criteria that cannot be tested by these data. However, previous studies have shown the presence of strong bottom flows in a few different locations in the ACC. The visual correspondence between the f/H field and mean flow features seen here leads us to believe that even in this relatively smooth and deep region of the ACC, the bottom exerts a strong influence on the flow.

Quantifying the isopycnal stirring was one of the main motivations behind the DIMES float experiment. The floats provide the first ground truth of the of the stirring processes at work. They clearly show the presence of jets in the flow and strongly suggest that they form transport barriers, with the strength of these barriers decreasing with depth. The regions between the jets are well mixed and the diffusivities in these regions decreases with depth, following the general decrease of EKE with depth and in accordance with mean flow suppression. The long-time asymptote of diffusivity in the Southeast Pacific ocean shows stronger mixing at depth, with cross stream diffusivities of $500m^2/s$ between 500-1400m and $1100m^2/s$ between 1400-2500m.

There are fewer data in the Scotia Sea; this lack of data produces noisier estimates, with average cross stream diffusivity of approximately $1200m^2/s$ both in the shallow and deep bins. The results for the Scotia Sea are plagued not only by the scarcity of data but also by the presence of an extremely complex mean flow pattern. The complex mountain ranges present in this region can guide flow in the deeper layers significantly different from the flow above, leading to mean currents that cross the core of the ACC. One example of this is seen in the floats that continued east in the Scotia Sea, instead of crossing over the North Scotia Ridge into the Argentine Basin (Fig. 11). This dispersion or leakage can transport water across the major fronts of the ACC in a non-diffusive fashion.

The results here imply that the strong inhomogeneities exist in the diffusivities, related to jets and thin barriers to mixing within the broader ACC. This may have lead to disparate previous results based on the chosen averaging method. In an ideal case, with zonally homogeneous jets, a lagrangian estimate of meridional diffusivity should asymptote to the harmonic average of the diffusivities in the meridional direction (Nakamura (2008), see also Thompson and Sallée (2012)). The ACC is not zonally homogeneous and in most regions the jets are transient features of flow that do indeed merge and split. In such a complex system, it is not clear yet that a simple measure of mixing is appropriate. Using lagrangian observational methods, however, we are able to reveal some of this complexity and point to dynamical structure in the flow that controls mixing. There remains a gap in our understanding of the relation between large-scale flow quantities and relevant eddy diffusivities, hindering the development of parameterizations of eddy diffusivities in complex flow.

Acknowledgments. We thank captains and the crews of US1 2009 R/V Roger Revelle, US2 2010 R/V Thomas G. Thompson, UK1 2009 James Cook, UK2 2010 James Cook, UK3 James Cook, UK4 2012 James Clark Ross all of which contributed to the success of the isopycnal (float) component of DIMES, for their willing help and support. The marine operations groups of SIO, UW, BAS, NERC were of utmost importance for their professional work and willing support at sea in good and in difficult weather. DB and KS would like to acknowledge support from NSF OCE 1231803, NSF OCE 0622670 and NSF OCE 0822075.

References

Abernathey, R., J. Marshall, M. Mazloff, and E. Shuckburgh, 2010: Enhancement of mesoscale eddy stirring at steering levels in the Southern Ocean. *Journal of Physical Oceanography*, **40 (1)**, 170–184.

Balwada, D., K. G. Speer, and J. R. Ledwell, 2015: A Lagrangian view of the Antarctic Circumpolar Current in the Southeast Pacific Ocean and Scotia Sea. *to be submitted*.

Barré, N., C. Provost, A. Renault, and N. Sennéchael, 2011: Fronts, meanders and eddies in Drake Passage during the ANT-XXIII/3 cruise in January–February 2006: A satellite perspective. *Deep Sea Research Part II: Topical Studies in Oceanography*, **58 (25)**, 2533–2554.

Bates, M., R. Tulloch, J. Marshall, and R. Ferrari, 2014: Rationalizing the spatial distribution of mesoscale eddy diffusivity in terms of mixing length theory. *Journal of Physical Oceanography*, **44 (6)**, 1523–1540, doi:10.1175/JPO-D-13-0130.1, URL http://dx.doi.org/10.1175/JPO-D-13-0130.1.

Brearley, J. A., K. L. Sheen, A. C. Naveira Garabato, D. A. Smeed, K. G. Speer, A. M. Thurnherr, M. P. Meredith, and S. Waterman, 2014: Deep boundary current disintegration in Drake Passage. *Geophysical Research Letters*, **41 (1)**, 121–127, doi:10.1002/2013GL058617, URL http://dx.doi.org/10.1002/2013GL058617, 2013GL058617.

Chelton, D. B., M. G. Schlax, and R. M. Samelson, 2011: Global observations of nonlinear mesoscale eddies. *Progress in Oceanography*, **91 (2)**, 167–216.

Chen, R., S. T. Gille, J. L. McClean, G. R. Flierl, and A. Griesel, 2015: A multi-wavenumber theory for eddy diffusivities and its application to the southeast Pacific (DIMES) region. *Journal of Physical Oceanography*, doi:10.1175/JPO-D-14-0229.1, URL http://dx.doi.org/10.1175/JPO-D-14-0229.1.

Chereskin, T. K., K. A. Donohue, and D. R. Watts, 2012: cDrake: Dynamics and transport of the Antarctic Circumpolar Current in Drake Passage. *Oceanography*, **25 (3)**, 134–135.

Davis, R. E., 1991: Observing the general circulation with floats. *Deep Sea Research Part A. Oceanographic Research Papers*, **38**, S531–S571.

Faure, V., and K. Speer, 2012: Deep circulation in the Eastern South Pacific Ocean. *Journal of Marine Research*, **70 (5)**, 748–778, doi:doi:10.1357/002224012806290714, URL http://www.ingentaconnect.com/content/jmr/jmr/2012/00000070/00000005/art00003.

Ferrari, R., and M. Nikurashin, 2010: Suppression of eddy diffusivity across jets in the Southern Ocean. *Journal of Physical Oceanography*, **40 (7)**, 1501–1519.

Ferrari, R., C. Provost, A. Renault, N. Sennéchael, N. Barré, Y.-H. Park, and J. H. Lee, 2012: Circulation in Drake Passage revisited using new current time series and satellite altimetry: 1. The Yaghan Basin. *Journal of Geophysical Research: Oceans (1978–2012)*, **117 (C12)**.

Ferrari, R., C. Provost, N. Sennéchael, and J.-H. Lee, 2013: Circulation in Drake Passage revisited using new current time series and satellite altimetry: 2. The Ona Basin. *Journal of Geophysical Research: Oceans*.

Firing, Y. L., T. K. Chereskin, and M. R. Mazloff, 2011: Vertical structure and transport of the Antarctic Circumpolar Current in Drake Passage from direct velocity observations. *Journal of Geophysical Research*, **116 (C8)**, C08 015.

Freeland, H., P. Rhines, and T. Rossby, 1975: Statistical observations of the trajectories of neutrally buoyant floats in the North Atlantic. *Journal of Marine Research*, **33 (3)**, 383–404.

Fu, L.-L., 2009: Pattern and velocity of propagation of the global ocean eddy variability. *Journal of Geophysical Research*, **114 (C11017)**.

Garabato, A. C. N., A. P. Williams, and S. Bacon, 2014: The three-dimensional overturning circulation of the Southern Ocean during the WOCE era. *Progress in Oceanography*, **120**, 41 – 78, doi:http://dx.doi.org/10.1016/j.pocean.2013.07.018, URL http://www.sciencedirect.com/science/article/pii/S0079661113001316.

Garraffo, Z. D., A. J. Mariano, A. Griffa, C. Veneziani, and E. P. Chassignet, 2001: Lagrangian data in a high-resolution numerical simulation of the North Atlantic: I. comparison with in situ drifter data. *Journal of Marine Systems*, **29 (1)**, 157–176.

Gille, S. T., 2003a: Float observations of the Southern Ocean. Part I: Estimating mean fields, bottom velocities, and topographic steering. *Journal of Physical Oceanography*, **33 (6)**, 1167–1181.

Gille, S. T., 2003b: Float observations of the Southern Ocean. part II: Eddy fluxes. *Journal of Physical Oceanography*, **33 (6)**, 1182–1196.

Gille, S. T., K. Speer, J. R. Ledwell, and A. C. Naveira Garabato, 2007: Mixing and stirring in the Southern Ocean. *Eos, Transactions American Geophysical Union*, **88 (39)**, 382–383.

Hancock, C., and K. Speer, 2013a: Critical layers and isopycnal mixing in the Southern Ocean RAFOS float data report February 2010-February 2012. *FSU Marine Field Group Report 13-1*.

Hancock, C., and K. Speer, 2013b: Diapycnal and Isopyncal Mixing Experiment in the Southern Ocean RAFOS float data report February 2009-February 2012. *FSU Marine Field Group Report 13-2*.

Hughes, C. W., 2005: Nonlinear vorticity balance of the Antarctic Circumpolar Current. *Journal of Geophysical Research: Oceans*, **110 (C11)**, n/a–n/a, doi:10.1029/2004JC002753, URL http://dx.doi.org/10.1029/2004JC002753, c11008.

Hughes, C. W., and P. D. Killworth, 1995: Effects of bottom topography in the large-scale circulation of the Southern Ocean. *Journal of Physical Oceanography*, **25 (11)**, 2485–2497, doi:10.1175/1520-0485(1995)025⟨2485:EOBTIT⟩2.0.CO;2, URL http://dx.doi.org/10.1175/1520-0485(1995)025⟨2485:EOBTIT⟩2.0.CO;2.

Karsten, R. H., and J. Marshall, 2002: Testing theories of the vertical stratification of the ACC against observations. *Dynamics of Atmospheres and Oceans*, **36 (1)**, 233–246.

Killworth, P., 1992: An equivalent-barotropic mode in the fine resolution model. *Journal of Physical Oceanography*, **21 (1)**, 1379–1387.

Klocker, A., R. Ferrari, and J. H. LaCasce, 2012: Estimating suppression of eddy mixing by mean flows. *Journal of Physical Oceanography*, **42 (9)**, 1566–1576.

LaCasce, J., 2000: Floats and f/H. *Journal of marine research*, **58 (1)**, 61–95.

LaCasce, J., 2008: Statistics from lagrangian observations. *Progress in Oceanography*, **77 (1)**, 1–29.

LaCasce, J., R. Ferrari, J. Marshall, R. Tulloch, D. Balwada, and K. Speer, 2014: Float-derived isopycnal diffusivities in the DIMES experiment. *Journal of Physical Oceanography*, **44 (2)**, 764–780.

LaCasce, J., and P. Isachsen, 2010: The linear models of the ACC. *Progress in Oceanography*, **84 (3)**, 139–157.

Lenn, Y., T. Chereskin, J. Sprintall, and E. Firing, 2007: Mean jets, mesoscale variability and eddy momentum fluxes in the surface layer of the Antarctic Circumpolar Current in Drake Passage. *Journal of Marine Research*, **65 (1)**, 27–58.

Lenn, Y.-D., T. K. Chereskin, and J. Sprintall, 2008: Improving estimates of the Antarctic Circumpolar Current streamlines in Drake Passage. *Journal of Physical Oceanography*, **38 (5)**, 1000–1010.

Lu, J., and K. Speer, 2010: Topography, jets, and eddy mixing in the Southern Ocean. *Journal of Marine Research*, **68 (3-4)**, 3–4.

Lumpkin, R., and K. Speer, 2007: Global ocean meridional overturning. *Journal of Physical Oceanography*, **37 (10)**, 2550–2562, doi:10.1175/JPO3130.1, URL http://dx.doi.org/10.1175/JPO3130.1.

Lumpkin, R., A.-M. Treguier, and K. Speer, 2002: Lagrangian eddy scales in the Northern Atlantic ocean. *Journal of Physical Oceanography*, **32 (9)**, 2425–2440, doi:10.1175/1520-0485(2002)032⟨2425:LESITN⟩2.0.CO;2, URL http://journals.ametsoc.org/doi/abs/10.1175/1520-0485%282002%29032%3C2425%3ALESITN%3E2.0.CO%3B2.

Marshall, J., D. Olbers, H. Ross, and D. Wolf-Gladrow, 1993: Potential vorticity constraints on the dynamics and hydrography of the Southern Ocean. *Journal of Physical Oceanography*, **23 (3)**, 465–487.

Marshall, J., E. Shuckburgh, H. Jones, and C. Hill, 2006: Estimates and implications of surface eddy diffusivity in the Southern Ocean derived from tracer transport. *Journal of Physical Oceanography*, **36 (9)**, 1806–1821.

Marshall, J., and K. Speer, 2012: Closure of the meridional overturning circulation through Southern Ocean upwelling. *Nature Geoscience*.

McCartney, M., 1976: The interaction of zonal currents with topography with applications to the Southern Ocean. *Deep Sea Research*, **23**, 413–427.

Meredith, M. P., and Coauthors, 2011: Sustained monitoring of the Southern Ocean at Drake Passage: Past achievements and future priorities. *Reviews of Geophysics*, **49 (4)**.

Middleton, J. F., 1985-02-01T00:00:00: Drifter spectra and diffusivities. *Journal of Marine Research*, **43 (1)**, 37–55, URL http://www.ingentaconnect.com/content/jmr/jmr/1985/00000043/00000001/art00003.

Nakamura, N., 2008: Sensitivity of global mixing and fluxes to isolated transport barriers. *Journal of the Atmospheric Sciences*, **65 (12)**, 3800–3818, doi:10.1175/2008JAS2641.1, URL http://dx.doi.org/10.1175/2008JAS2641.1.

Naveira Garabato, A. C., R. Ferrari, and K. L. Polzin, 2011: Eddy stirring in the Southern Ocean. *Journal of Geophysical Research: Oceans (1978–2012)*, **116 (C9)**.

Nowlin, W. D., and J. M. Klinck, 1986: The physics of the Antarctic Circumpolar Current. *Reviews of Geophysics*, **24 (3)**, 469–491.

Olbers, D., D. Borowski, C. Voelcker, and J.-O. Woelff, 2004: The dynamical balance, transport and circulation of the Antarctic Circumpolar Current. *Antarctic science*, **16 (4)**, 439–470.

Ollitrault, M., and A. Colin de Verdière, 2002: SOFAR floats reveal midlatitude intermediate North Atlantic general circulation. Part II: An eulerian statistical view. *Journal of Physical Oceanography*, **32 (7)**, 2034–2053, doi:10.1175/1520-0485(2002)032⟨2034:SFRMIN⟩2.0.CO;2, URL http://dx.doi.org/10.1175/1520-0485(2002)032⟨2034:SFRMIN⟩2.0.CO;2.

Orsi, A. H., T. Whitworth, and W. D. Nowlin, 1995: On the meridional extent and fronts of the Antarctic Circumpolar Current. *Deep Sea Research Part I: Oceanographic Research Papers*, **42 (5)**, 641–673.

Phillips, H. E., and N. L. Bindoff, 2014: On the nonequivalent barotropic structure of the Antarctic Circumpolar Current: An observational perspective. *Journal of Geophysical Research: Oceans*, **119 (8)**, 5221–5243, doi:10.1002/2013JC009516, URL http://dx.doi.org/10.1002/2013JC009516.

Phillips, H. E., and S. R. Rintoul, 2000: Eddy variability and energetics from direct current measurements in the Antarctic Circumpolar Current south of Australia. *Journal of Physical Oceanography*, **30 (12)**, 3050–3076.

Pillsbury, R. D., T. Whitworth III, W. D. Nowlin Jr, and F. Sciremammano Jr, 1979: Currents and temperatures as observed in Drake Passage during 1975. *Journal of Physical Oceanography*, **9 (3)**, 469–482.

R Rintoul, S., C. W Hughes, and D. Olbers, 2001: The Antarctic Circumpolar Current system. *International Geophysics*, **77**, 271–XXXVI.

Rossby, T., D. Dorson, and J. Fontaine, 1986: The RAFOS system. *Journal of Atmospheric and Oceanic Technology*, **3 (4)**, 672–679.

Rupolo, V., V. Artale, B. L. Hua, and A. Provenzale, 1996: Lagrangian velocity spectra at 700 m in the western north atlantic. *Journal of Physical Oceanography*, **26 (8)**, 1591–1607, doi:10.1175/1520-0485(1996)026⟨1591:LVSAMI⟩2.0.CO;2, URL http://dx.doi.org/10.1175/1520-0485(1996)026⟨1591:LVSAMI⟩2.0.CO;2.

Sallée, J., K. Speer, and R. Morrow, 2008a: Southern ocean fronts and their variability to climate modes. *J. Clim*, **21 (12)**, 3020–3039.

Sallée, J., K. Speer, R. Morrow, and R. Lumpkin, 2008b: An estimate of lagrangian eddy statistics and diffusion in the mixed layer of the Southern Ocean. *Journal of Marine Research*, **66 (4)**, 441–463.

Sloyan, B. M., and S. R. Rintoul, 2001: The southern ocean limb of the global deep overturning circulation*. *Journal of Physical Oceanography*, **31 (1)**, 143–173, doi:10.1175/1520-0485(2001)031⟨0143:TSOLOT⟩2.0.CO;2, URL http://dx.doi.org/10.1175/1520-0485(2001)031⟨0143:TSOLOT⟩2.0.CO;2.

Sokolov, S., and S. R. Rintoul, 2007: Multiple jets of the Antarctic Circumpolar Current South of Australia. *Journal of Physical Oceanography*, **37 (5)**, 1394–1412.

Sokolov, S., and S. R. Rintoul, 2009: Circumpolar structure and distribution of the Antarctic Circumpolar Current fronts: 1. Mean circumpolar paths. *Journal of Geophysical Research: Oceans (1978–2012)*, **114 (C11)**.

Sommeria, J., S. D. Meyers, and H. L. Swinney, 1989: Laboratory model of a planetary eastward jet. *Nature*, **337 (6202)**, 58–61, URL http://dx.doi.org/10.1038/337058a0.

Swenson, M. S., and P. P. Niiler, 1996: Statistical analysis of the surface circulation of the California Current. *Journal of Geophysical Research: Oceans*, **101 (C10)**, 22 631–22 645, doi:10.1029/96JC02008, URL http://dx.doi.org/10.1029/96JC02008.

Talley, L., 2013: Closure of the global overturning circulation through the Indian, Pacific, and Southern oceans: Schematics and transports. *Oceanography*, **26 (1)**, 80–97.

Taylor, G., 1921: Diffusion by continuous movements. *Proc. Lond. Math. Soc. Series*, **20**, 196–212.

Thompson, A. F., 2010: Jet formation and evolution in baroclinic turbulence with simple topography. *Journal of Physical Oceanography*, **40 (2)**, 257–278, doi:10.1175/2009JPO4218.1, URL http://dx.doi.org/10.1175/2009JPO4218.1.

Thompson, A. F., P. H. Haynes, C. Wilson, and K. J. Richards, 2010: Rapid Southern Ocean front transitions in an eddy-resolving ocean GCM. *Geophysical Research Letters*, **37 (23)**, n/a–n/a, doi:10.1029/2010GL045386, URL http://dx.doi.org/10.1029/2010GL045386, l23602.

Thompson, A. F., and J.-B. Sallée, 2012: Jets and topography: Jet transitions and the impact on transport in the Antarctic Circumpolar Current. *Journal of Physical Oceanography*, **42 (6)**, 956–972, doi:10.1175/JPO-D-11-0135.1, URL http://dx.doi.org/10.1175/JPO-D-11-0135.1.

Tulloch, R., and Coauthors, 2014: Direct estimate of lateral eddy diffusivity upstream of Drake Passage. *Journal of Physical Oceanography*, **44 (10)**, 2593–2616, doi:10.1175/JPO-D-13-0120.1, URL http://dx.doi.org/10.1175/JPO-D-13-0120.1.

Warren, B. A., 1990: Suppression of deep oxygen concentrations by Drake Passage. *Deep Sea Research Part A. Oceanographic Research Papers*, **37 (12)**, 1899 – 1907, doi:http://dx.doi.org/10.1016/0198-0149(90)90085-A, URL http://www.sciencedirect.com/science/article/pii/019801499090085A.

LIST OF TABLES

Table 1. Statistics for DIMES RAFOS floats in six longitudinal and depth bins 39

TABLE 1: Statistics for DIMES RAFOS floats in six longitudinal and depth bins

Longitude bins	110^oW-90^oW		90^oW-70^oW		70^oW-40^oW	
Depth bins	**500 - 1400m**	**1400 - 2500m**	**500 - 1400m**	**1400 - 2500m**	**500 - 1400m**	**1400 - 2500m**
$L^e_{uu}(km)$	75.09 ± 1.17	57.81 ± 0.79	61.09 ± 3.8	77.90 ± 6.64	57.47 ± 3.16	56.60 ± 9.62
$L^e_{vv}(km)$	92.03 ± 1.5	59.97 ± 0.99	57.59 ± 2.35	77.11 ± 8.12	68.49 ± 5.12	62.22 ± 16.06
$L^e_{uu}(fit)(km)$	79.74 ± 0.78	57.55 ± 0.42	62.23 ± 1.92	58.28 ± 1.77	57.27 ± 1.89	40.27 ± 4.05
$L^e_{vv}(fit)(km)$	88.72 ± 0.82	55.52 ± 0.46	54.89 ± 1.15	68.10 ± 2.51	55.80 ± 2.09	36.15 ± 3.48
1^{st} zero crossing C^e_{uu}(km)	125.01	139.99	125.01	143.48	129.20	75.05
1^{st} zero crossing C^e_{vv}(km)	221.96	147.02	152.16	131.60	144.50	75.04
2^{nd} zero crossing C^e_{uu}(km)	239.83	225.07	175.68	225.06	247.73	175.15
2^{nd} zero crossing C^e_{vv}(km)	401.58	378.07	175.5	225.09	225.03	225.0
U(cm/s)	3.4 ± 0.33	2.25 ± 0.23	5.77 ± 0.65	3.83 ± 0.42	7.97 ± 1.38	6.68 ± 1.74
V(cm/s)	-0.6 ± 0.4	-0.51 ± 0.24	0.63 ± 0.64	0.01 ± 0.34	3.46 ± 1.43	2.4 ± 1.53
$c_{zonal}(cm/s)$	0.46 ± 0.98	0.46 ± 0.98	0.72 ± 0.86	0.72 ± 0.86	2.05 ± 1.73	2.05 ± 1.73
$c_{meridional}(cm/s)$	-0.18 ± 0.45	-0.18 ± 0.45	-0.07 ± 0.39	-0.07 ± 0.39	1.14 ± 1.41	1.14 ± 1.41
$u'u'(cm^2/s^2)$	35.45 ± 2.77	19.26 ± 1.4	80.14 ± 8.28	28.75 ± 3.16	215.5 ± 28.74	122.31 ± 27.14
$v'v'(cm^2/s^2)$	52.52 ± 4.1	21.94 ± 1.6	75.93 ± 7.84	26.27 ± 2.89	230.05 ± 30.68	94.57 ± 20.99
$T^l_{uu}(days)$	11.62 ± 1.58	10.98 ± 1.6	9.67 ± 1.68	12.72 ± 1.39	4.07 ± 0.82	5.89 ± 0.54
$T^l_{vv}(days)$	5.63 ± 0.74	7.77 ± 0.84	4.66 ± 0.64	6.29 ± 0.75	1.98 ± 0.44	3.35 ± 0.51
$T_{euu}(days)$	11.72 ± 1.59	13.14 ± 1.58	9.74 ± 1.63	12.95 ± 1.25	4.1 ± 0.68	9.35 ± 2.32
$T_{evv}(days)$	14.43 ± 2.42	15.52 ± 2.45	7.65 ± 1.31	11.7 ± 1.43	4.14 ± 0.69	7.96 ± 0.95
$T_{duu}(days)$	-	-	-	-	-	22 ± 28.7
$T_{dvv}(days)$	18.92 ± 14.94	26.47 ± 29.96	19.55 ± 50.99	26.39 ± 96.76	6.95 ± 15.12	10.86 ± 1.56
$T^{theory}_{duu}(days)$	126.81 ± 182.19	105.17 ± 162.85	47.61 ± 51.18	557.80 ± 3607.9	17.08 ± 14.89	28.58 ± 47.27
$T^{theory}_{dvv}(days)$	14.78 ± 5.32	18.69 ± 10.61	7.00 ± 1.59	14.50 ± 4.59	5.62 ± 2.14	7.07 ± 3.79
$K^o_{xx}(m^2/s)$	4425.3 ± 751.11	2350.2 ± 376.99	5858.7 ± 1293.6	3104.6 ± 563.3	7487.8 ± 1876.7	8563.2 ± 3406.3
$K^o_{yy}(m^2/s)$	5463.2 ± 1236.4	2773.4 ± 559.9	5027.3 ± 1099.3	2818.2 ± 560.8	7617.6 ± 1907.2	7416.6 ± 2510.1
$K_{xx}(m^2/s)$	4402.4 ± 768.4	1962.4 ± 345.1	5858.6 ± 1293.6	3049.1 ± 572.5	7092.7 ± 2118.9	5433.2 ± 1790
$K_{yy}(m^2/s)$	2132.2 ± 366.9	1391.1 ± 208.2	2821.1 ± 566.3	1496.8 ± 296.7	3475.8 ± 1072.8	3087.9 ± 1085.2

LIST OF FIGURES

Fig. 1. Regional geography with the major topographic features (bathymetry colored with contour spacing of 500 m), and experimental components. The 0 m and 3300 m depth contours are displayed in black and gray respectively to highlight the major topographic features. The yellow star is the tracer deployment location, the black dots are the float deployment locations and the red squares are the positions of the sound sources. SSH contours (-60cm and 20cm, dashed), which engulf the initial float deployment locations highlight the position of the ACC through the region. SAF and PF (solid black) from Orsi et al. (1995) 42

Fig. 2. Trajectories of the floats with mean depth greater than (a) 1400m (60 tracks) and (b) shallower than 1400m (80 tracks). The green dots represent the launch location and the red dots represent the surfacing location. 43

Fig. 3. Distribution of the total float days as a function of (a) calendar year, (b) pressure, (c) temperature and (d) height above topography. 44

Fig. 4. (a) Number of float days in $2.0^o X 0.5^o$ bins. (b) Number of floats that cross through a meridional bin normalized by the total number of floats that cross through the corresponding meridian. f/H contours are overlaid (gray) with f the Coriolis parameter and H the bathymetric depth 45

Fig. 5. Geostrophic velocities, calculated using SSH, compared with velocities from the floats. Probability distribution functions of ratio of float speed versus SSH derived speed plotted versus depth for (a) Southeast Pacific Ocean and (b) Scotia Sea respectively. Mode (solid lines), and mean (dashed lines) are given, error-bars represent one standard deviation; exponential fits (white lines) with depth scale of 1300m in the Scotia Sea and 1650m in the Southeast Pacific Ocean. Probability distribution function of the angle between SSH derived velocity and float velocity as a function of depth for (c) the Southeast Pacific Ocean and (d) Scotia Sea respectively; mean (solid) and one standard deviation (dashed). 46

Fig. 6. Probability distribution function of the ratio of float speed to SSH derived geostrophic speed binned in surface speed bins for (a) the Southeast Pacific Ocean and (b) Scotia Sea respectively. Probability distribution function of angle between SSH derived velocity and float velocity binned in surface speed bins for (a) Southeast Pacific Ocean and (b) Scotia Sea respectively; mean (solid) and one standard deviation (dashed). 47

Fig. 7. Vertical structure of (a) mean velocity in the Southeast Pacific Ocean (black) and Scotia Sea (blue), (b) EKE in the Southeast Pacific Ocean (black) and Scotia Sea (blue) binned in depth level bins. 'o' and '*' represent the zonal and meridional components respectively. 48

Fig. 8. Probability distribution functions of residual velocities in the (a) Southeast Pacific Ocean (b) Scotia Sea. The p values for the KS test to check gaussianity is shown in the legend. . . . 49

Fig. 9. 120 day segments of float tracks in the Southeast Pacific Ocean, showing loopers (a) and others (b). The way the distinction is made is described in the text. 50

Fig. 10. Binned eulerian fields for the Southeast Pacific Ocean. (a) Arrows indicate direction, mean speed is shaded. (b) EKE along with standard deviation ellipses. Barotropic PV (f/H) in the background corresponds to the depth field from Figure 9. 51

Fig. 11. Floats tracks in the Scotia Sea. (a) shows the loopers and (b) shows the non-loopers. The way the distinction is made is described in the text. 52

Fig. 12. Binned eulerian fields for the Scotia Sea. (a) Arrows indicate direction, mean speed is shaded. (b) EKE along with standard deviation ellipses. Barotropic PV (f/H) in the background corresponds to the depth field from Figure 11. 53

Fig. 13. Variance of the rate of change with time of the high frequency component of the pressure signal from the floats averaged for the two basins binned in the vertical (a; Southeast Pacific Ocean black, Scotia Sea blue) and geographically (b). 54

Fig. 14. Variance preserving lagrangian spectra from float velocity. Zonal velocity (solid line with dark shading) and meridional velocity (dashed with light shading). Errorbars are obtained by bootstrapping. 55

Fig. 15. Vertical structure of meridional diffusivity in the Southeast Pacific Ocean. The diffusivity scale $Ko = EKE.T_{evv}$ (blue) is calculated using only the decay time scale from the floats, the estimated value $K = EKE.T^{l}_{vv}$ (red) is calculated using the full lagrangian time scale from the floats and the value $K^{theory} = \frac{4EKET_{eij}T_{dij}^{theory2}}{\pi^2 T_{eij}^2 + 4T_{dij}^{theory2}}$ (black) is calculated using the decay time scale from the floats and meander time scale from theory, which assumed a length scale of 100km. 56

Fig. 16. Dispersion (a) and diffusivity (b) for the floats launched west of 100^oW in the Southeast Pacific Ocean divided into vertical bins encompassing 500-1400m and 1400-2500m. Dispersion (a) and diffusivity (b) for the floats that crossed 70^oW into the Scotia Sea and divided into vertical bins encompassing 500-1000 m and 1000-2500 m. 57

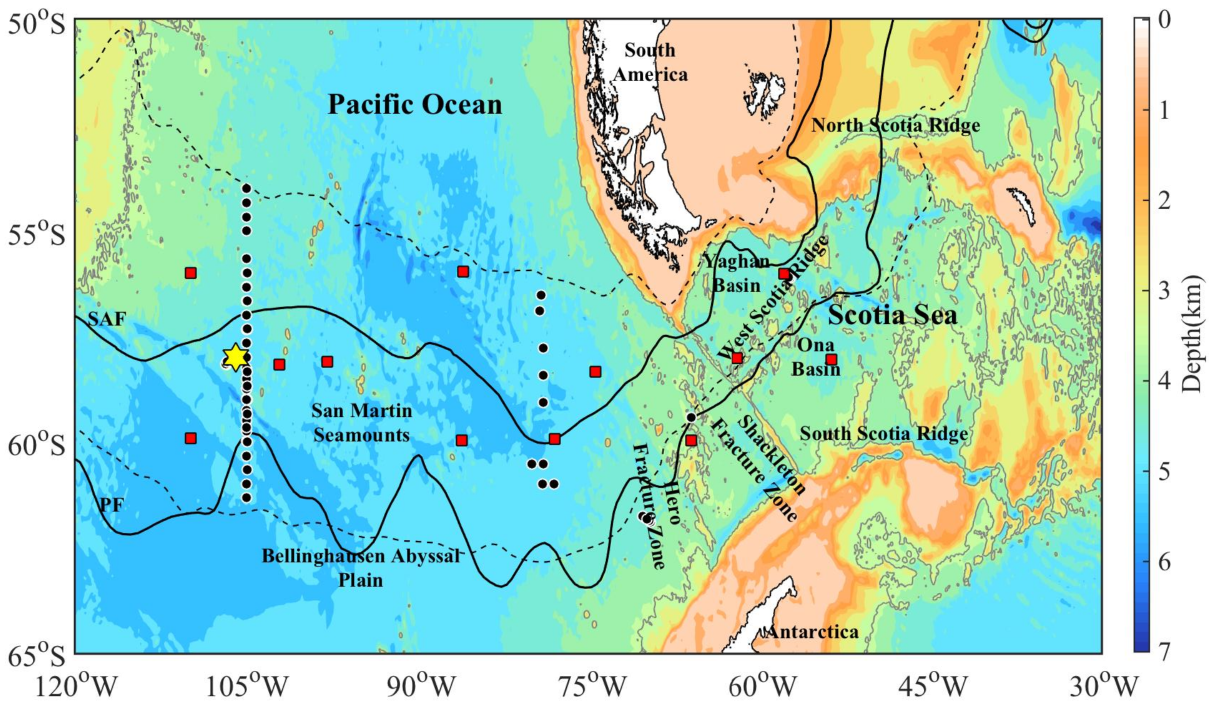

FIG. 1: Regional geography with the major topographic features (bathymetry colored with contour spacing of 500 m), and experimental components. The 0 m and 3300 m depth contours are displayed in black and gray respectively to highlight the major topographic features. The yellow star is the tracer deployment location, the black dots are the float deployment locations and the red squares are the positions of the sound sources. SSH contours (-60cm and 20cm, dashed), which engulf the initial float deployment locations highlight the position of the ACC through the region. SAF and PF (solid black) from Orsi et al. (1995)

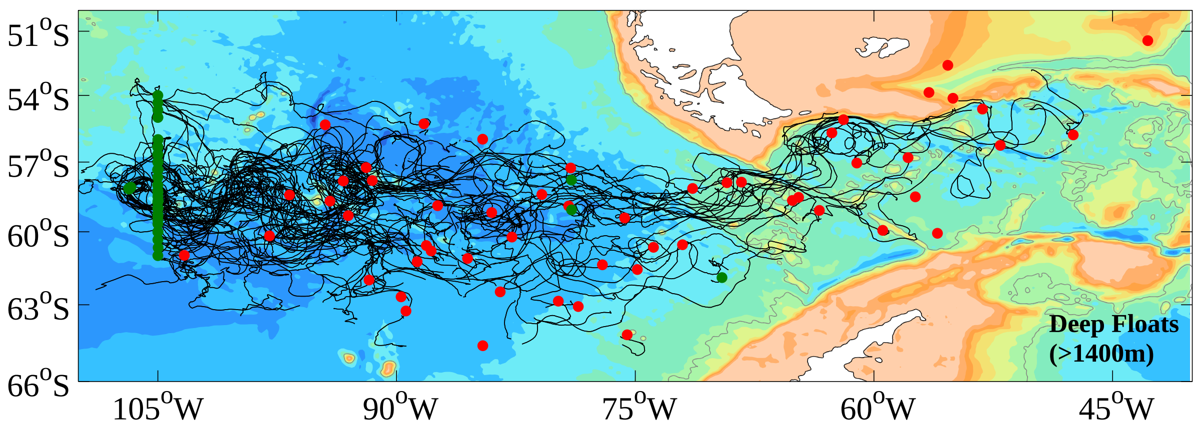

(a)

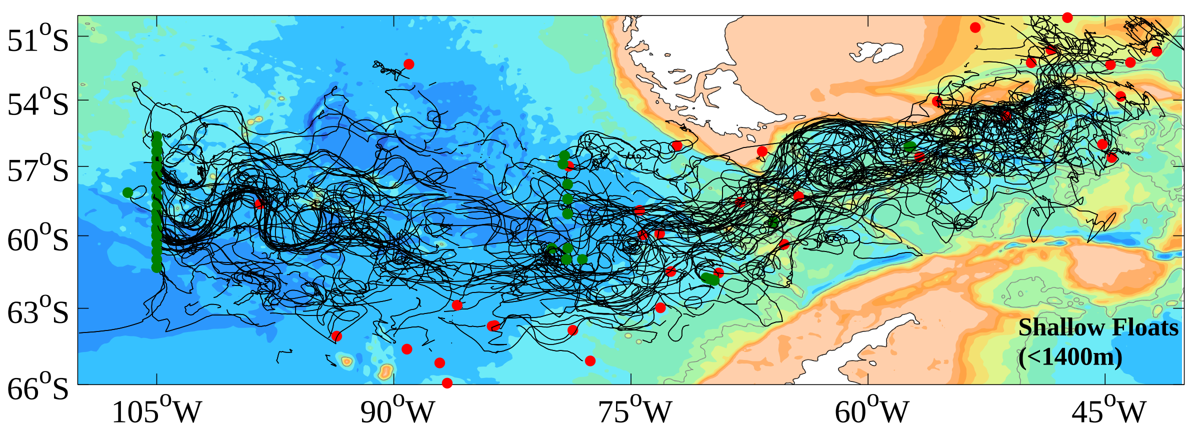

(b)

FIG. 2: Trajectories of the floats with mean depth greater than (a) 1400m (60 tracks) and (b) shallower than 1400m (80 tracks). The green dots represent the launch location and the red dots represent the surfacing location.

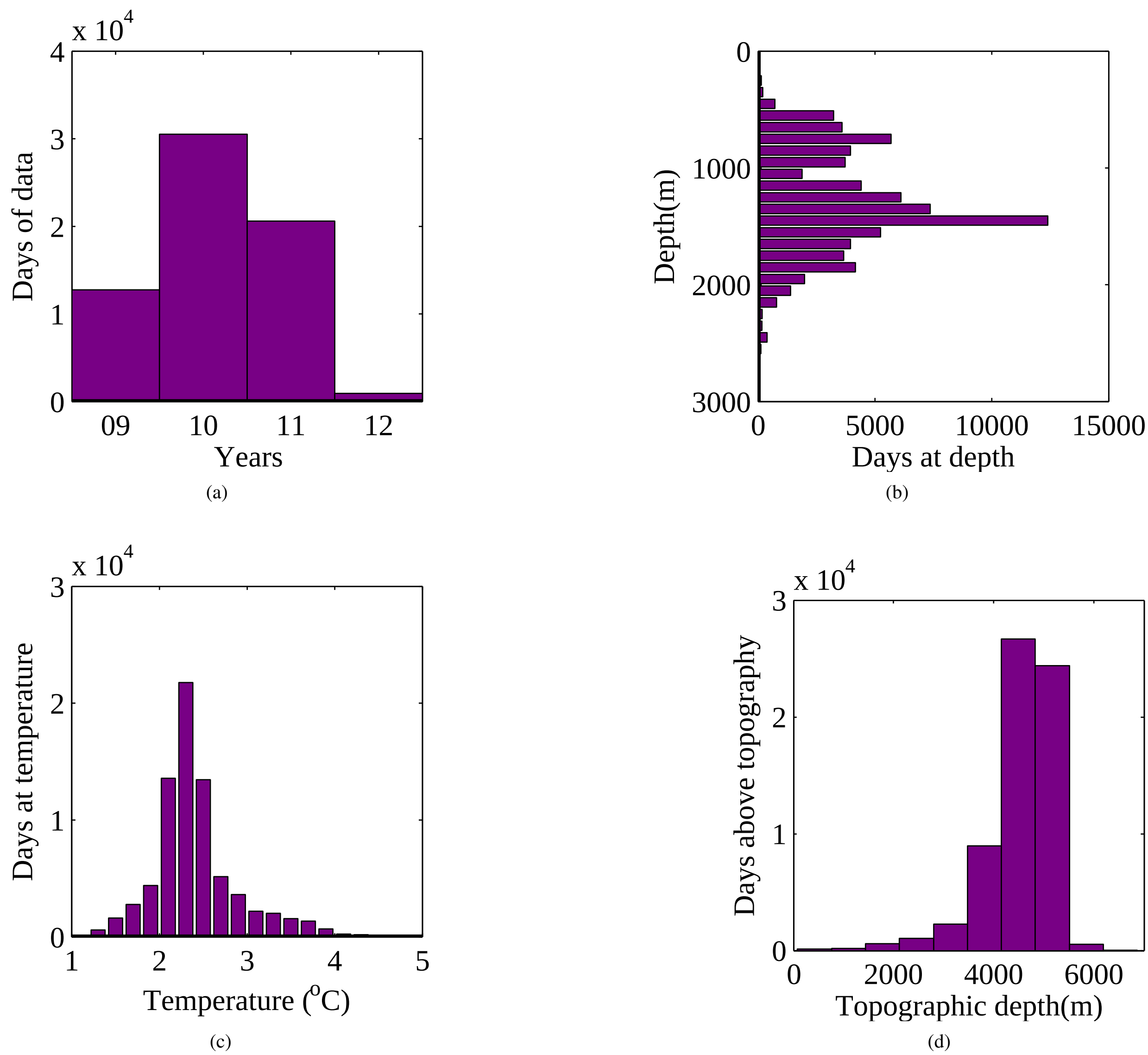

FIG. 3: Distribution of the total float days as a function of (a) calendar year, (b) pressure, (c) temperature and (d) height above topography.

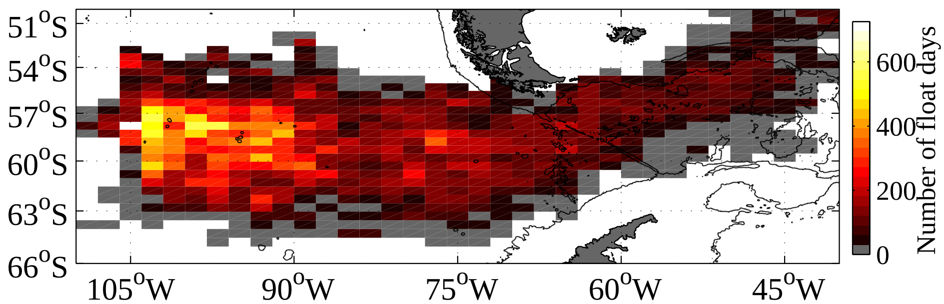

(a)

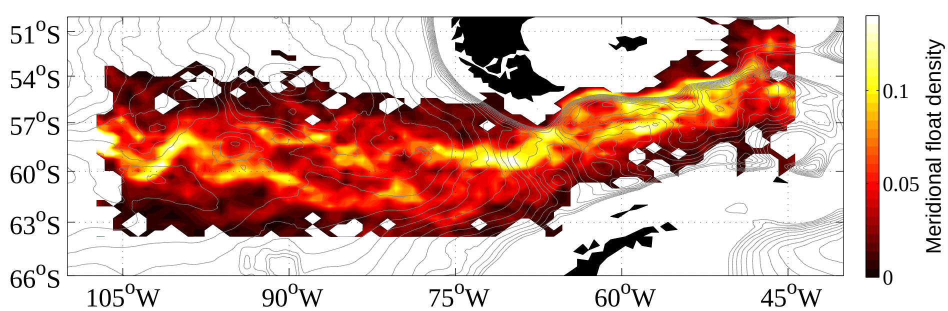

(b)

FIG. 4: (a) Number of float days in $2.0^o X 0.5^o$ bins. (b) Number of floats that cross through a meridional bin normalized by the total number of floats that cross through the corresponding meridian. f/H contours are overlaid (gray) with f the Coriolis parameter and H the bathymetric depth

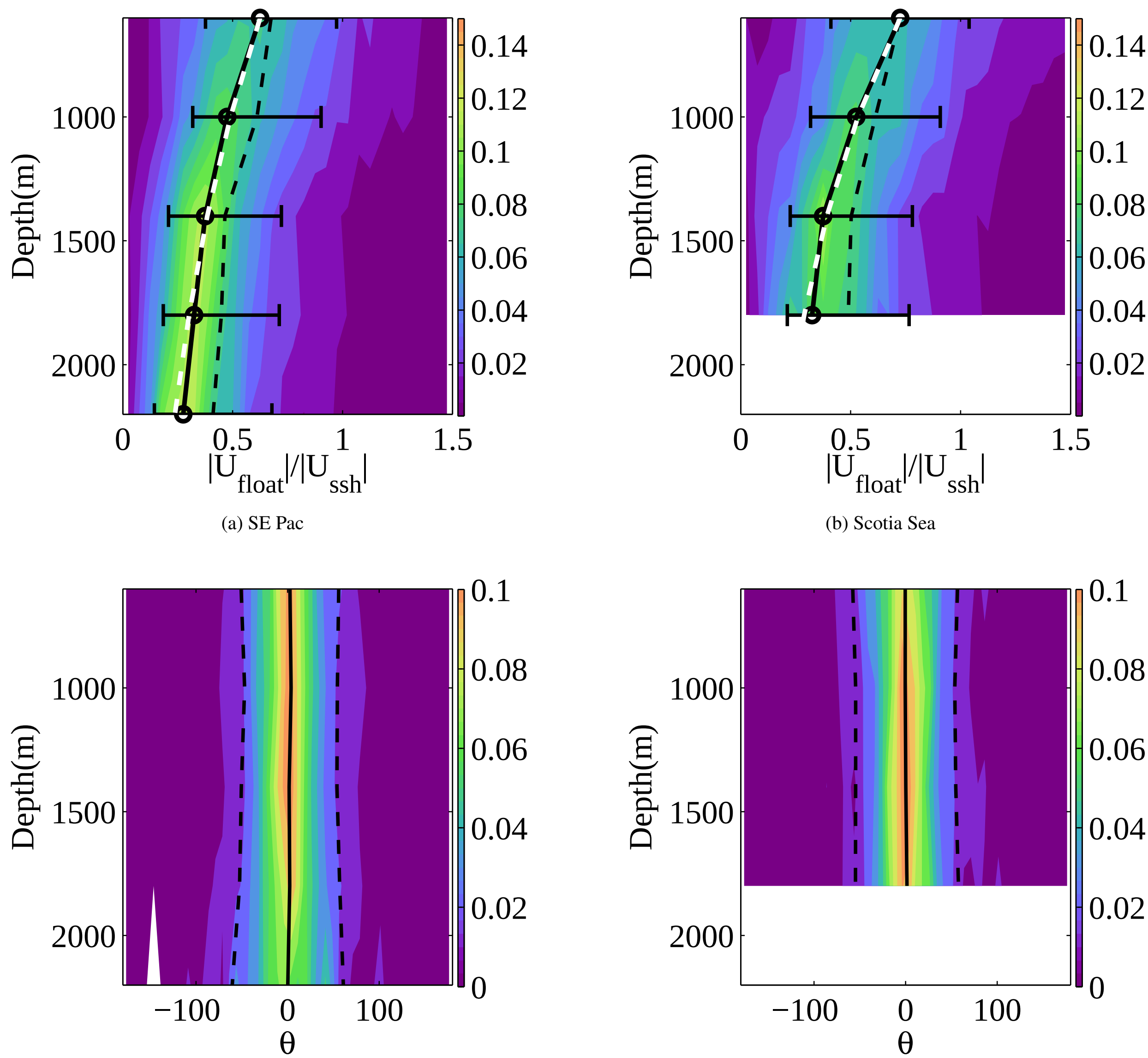

(a) SE Pac

(b) Scotia Sea

(c) SE Pac

(d) Scotia Sea

FIG. 5: Geostrophic velocities, calculated using SSH, compared with velocities from the floats. Probability distribution functions of ratio of float speed versus SSH derived speed plotted versus depth for (a) Southeast Pacific Ocean and (b) Scotia Sea respectively. Mode (solid lines), and mean (dashed lines) are given, error-bars represent one standard deviation; exponential fits (white lines) with depth scale of 1300m in the Scotia Sea and 1650m in the Southeast Pacific Ocean. Probability distribution function of the angle between SSH derived velocity and float velocity as a function of depth for (c) the Southeast Pacific Ocean and (d) Scotia Sea respectively; mean (solid) and one standard deviation (dashed).

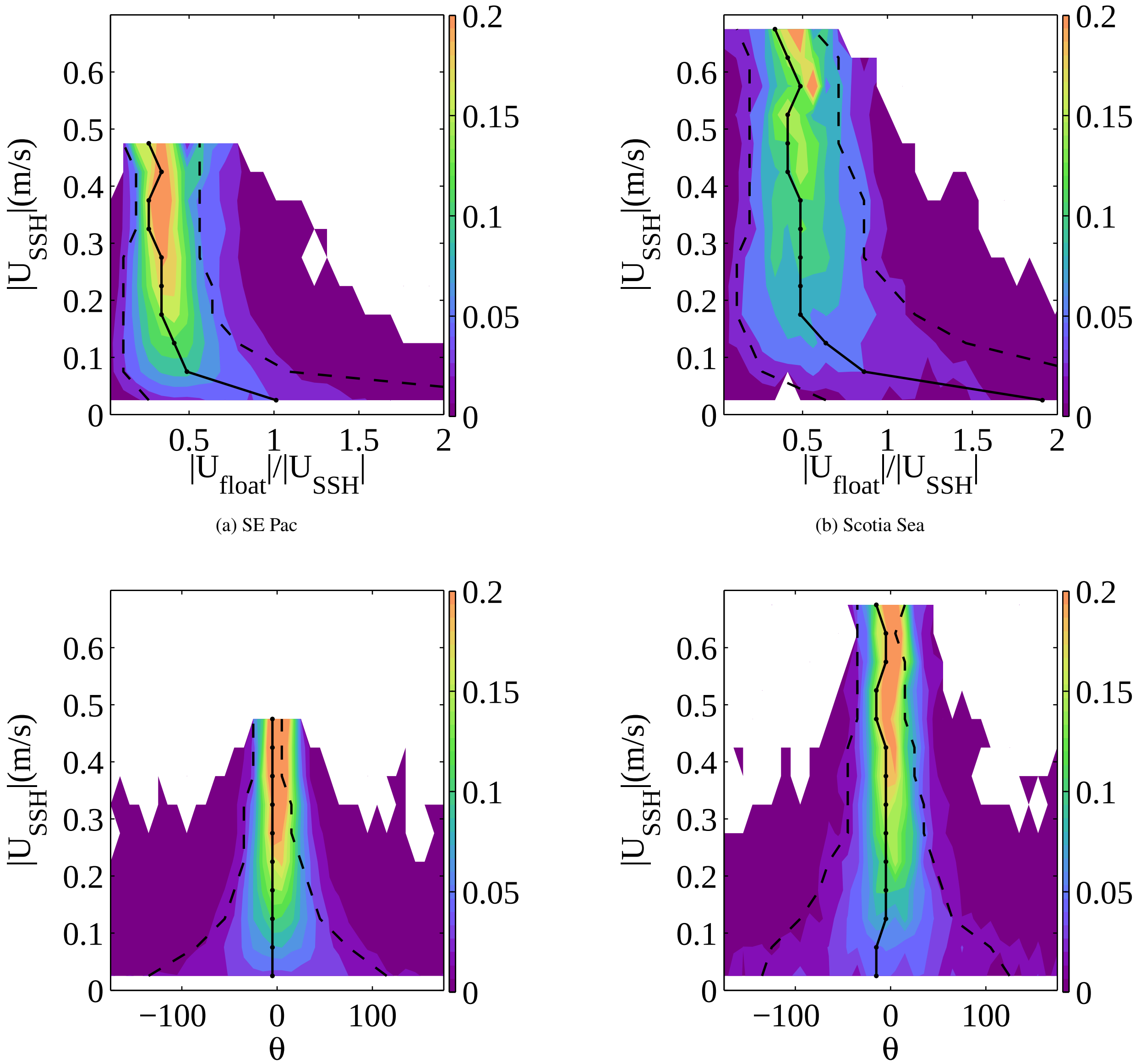

(a) SE Pac

(b) Scotia Sea

(c) SE Pac

(d) Scotia Sea

FIG. 6: Probability distribution function of the ratio of float speed to SSH derived geostrophic speed binned in surface speed bins for (a) the Southeast Pacific Ocean and (b) Scotia Sea respectively. Probability distribution function of angle between SSH derived velocity and float velocity binned in surface speed bins for (a) Southeast Pacific Ocean and (b) Scotia Sea respectively; mean (solid) and one standard deviation (dashed).

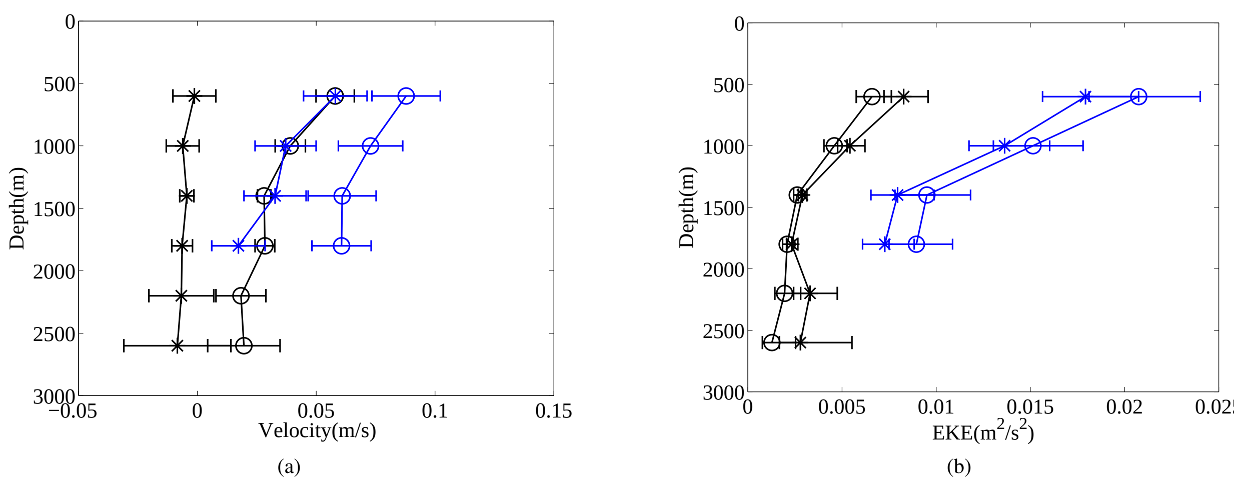

FIG. 7: Vertical structure of (a) mean velocity in the Southeast Pacific Ocean (black) and Scotia Sea (blue), (b) EKE in the Southeast Pacific Ocean (black) and Scotia Sea (blue) binned in depth level bins. 'o' and '*' represent the zonal and meridional components respectively.

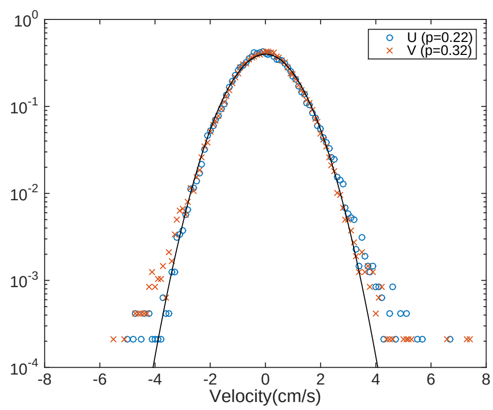

(a)

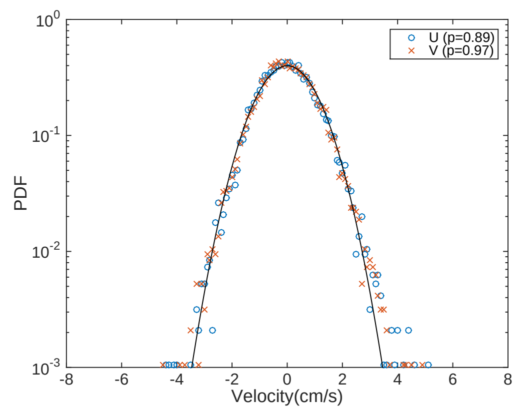

(b)

FIG. 8: Probability distribution functions of residual velocities in the (a) Southeast Pacific Ocean (b) Scotia Sea. The p values for the KS test to check gaussianity is shown in the legend.

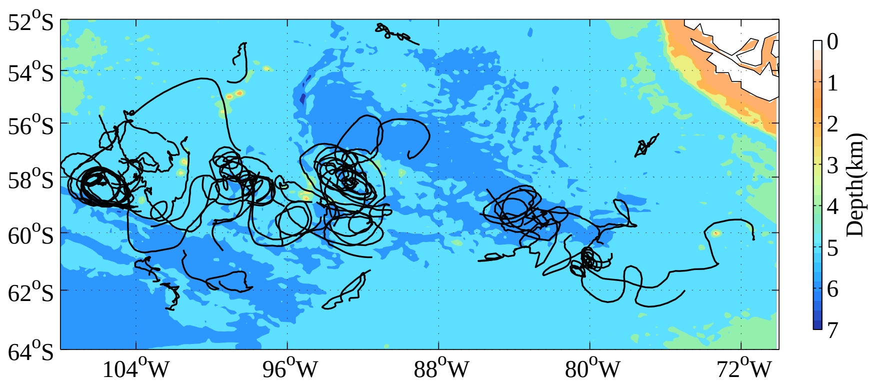

(a)

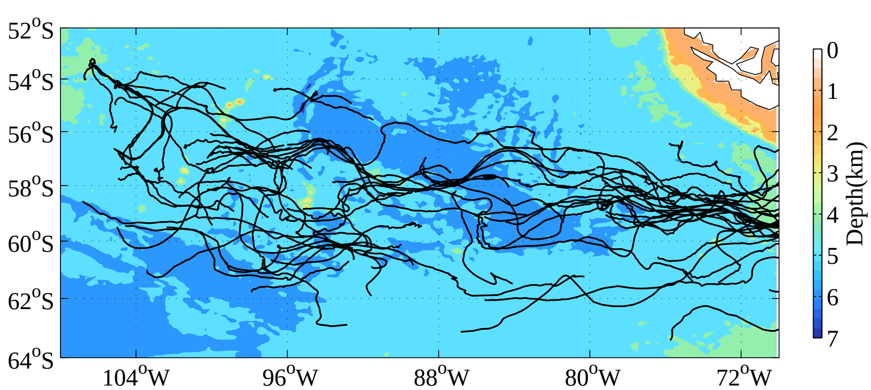

(b)

FIG. 9: 120 day segments of float tracks in the Southeast Pacific Ocean, showing loopers (a) and others (b). The way the distinction is made is described in the text.

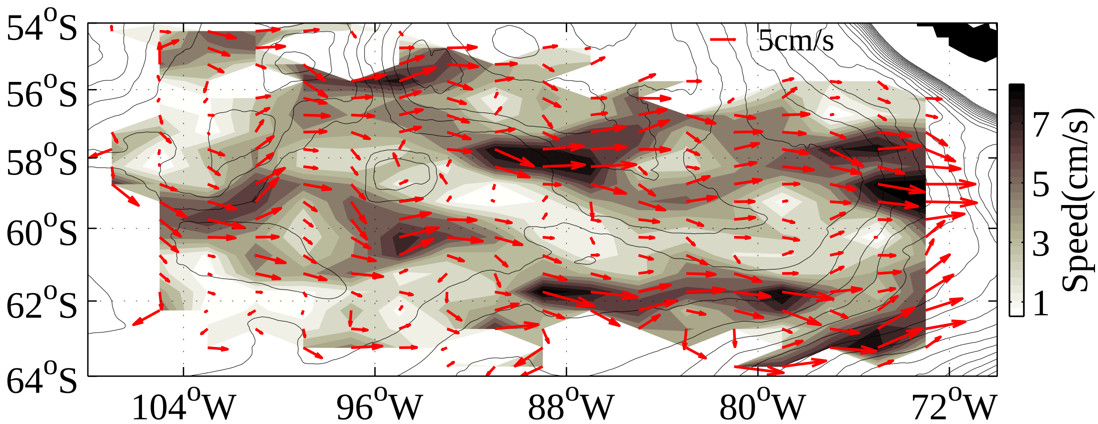

(a)

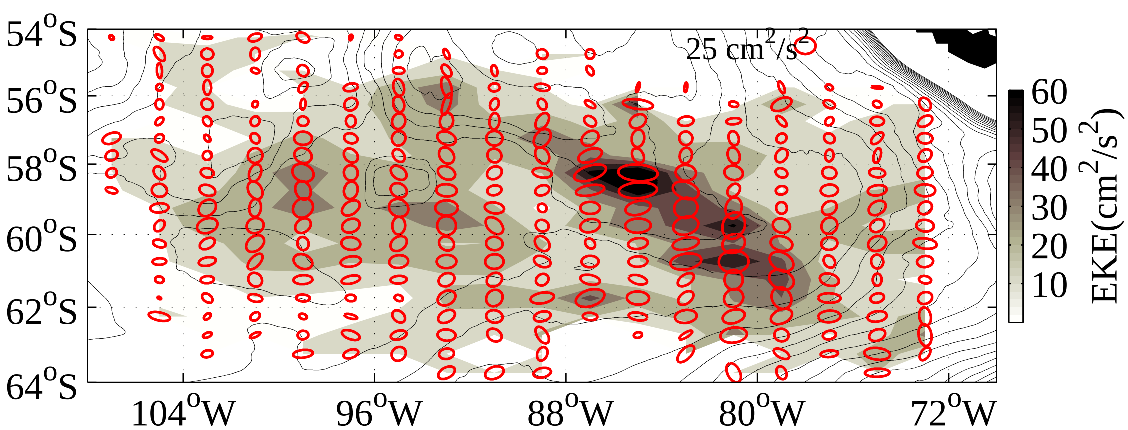

(b)

FIG. 10: Binned eulerian fields for the Southeast Pacific Ocean. (a) Arrows indicate direction, mean speed is shaded. (b) EKE along with standard deviation ellipses. Barotropic PV (f/H) in the background corresponds to the depth field from Figure 9.

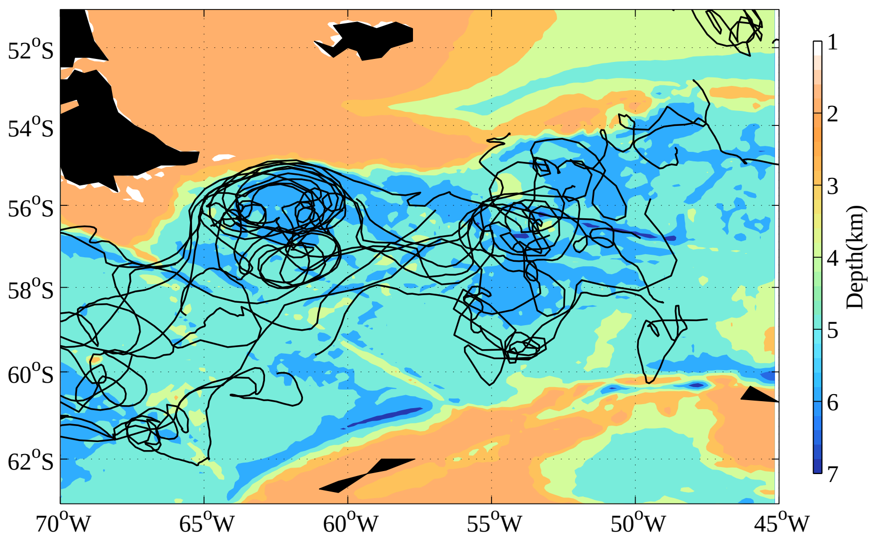

(a)

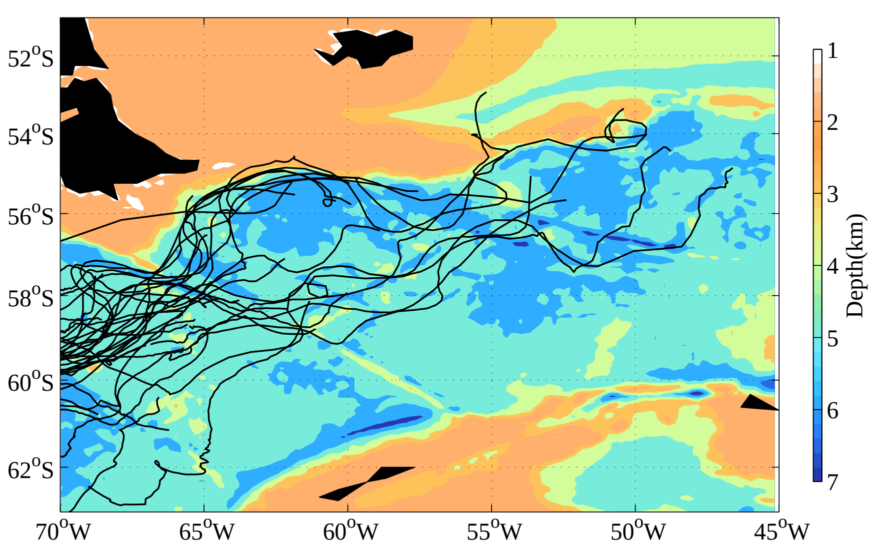

(b)

FIG. 11: Floats tracks in the Scotia Sea. (a) shows the loopers and (b) shows the non-loopers. The way the distinction is made is described in the text.

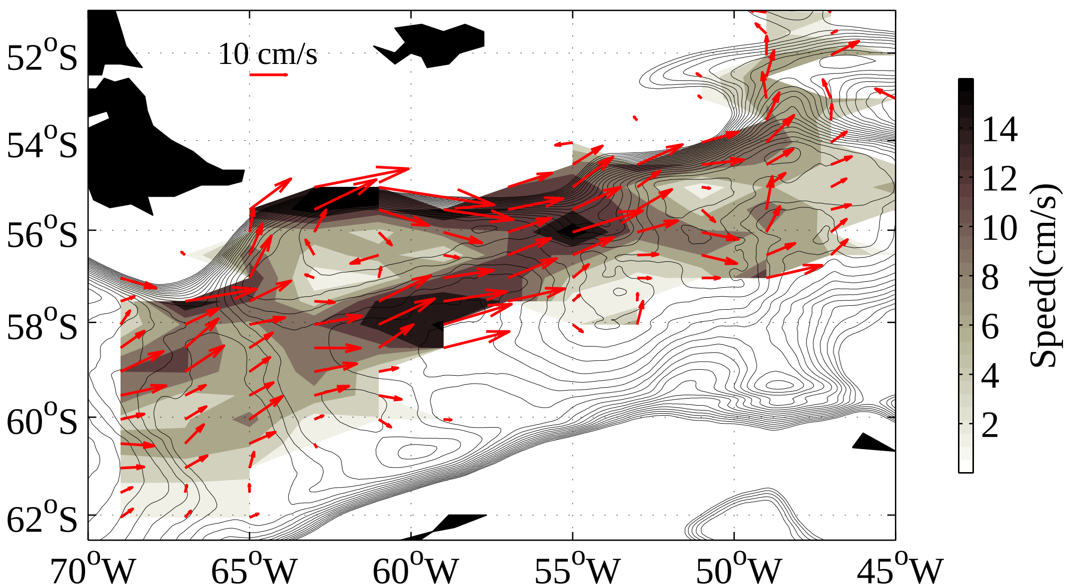

(a)

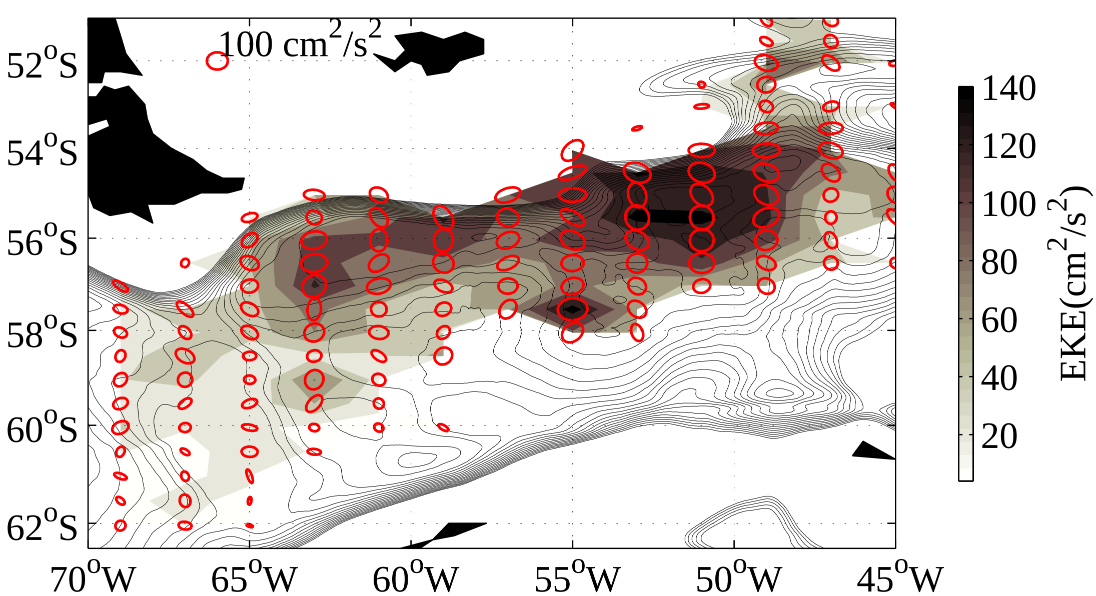

(b)

FIG. 12: Binned eulerian fields for the Scotia Sea. (a) Arrows indicate direction, mean speed is shaded. (b) EKE along with standard deviation ellipses. Barotropic PV (f/H) in the background corresponds to the depth field from Figure 11.

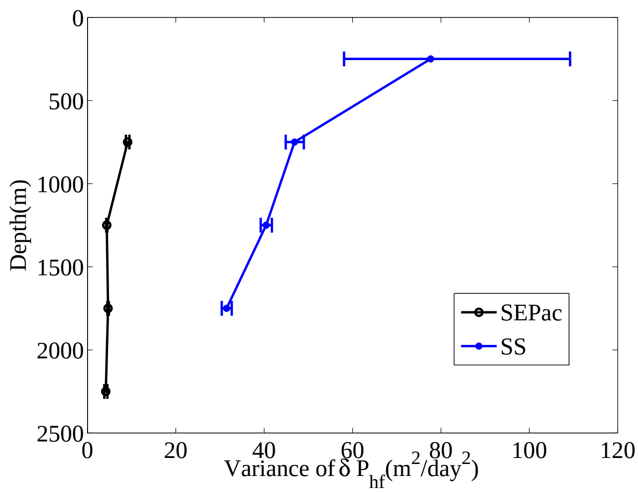

(a)

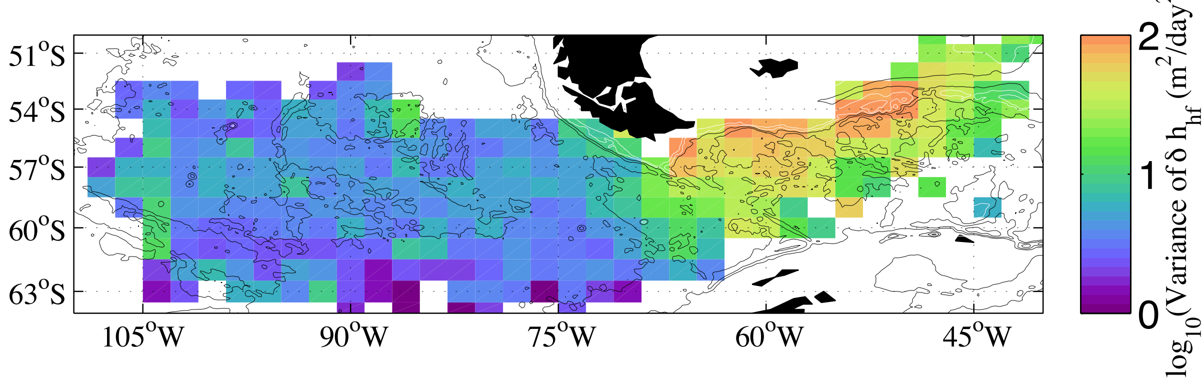

(b)

FIG. 13: Variance of the rate of change with time of the high frequency component of the pressure signal from the floats averaged for the two basins binned in the vertical (a; Southeast Pacific Ocean black, Scotia Sea blue) and geographically (b).

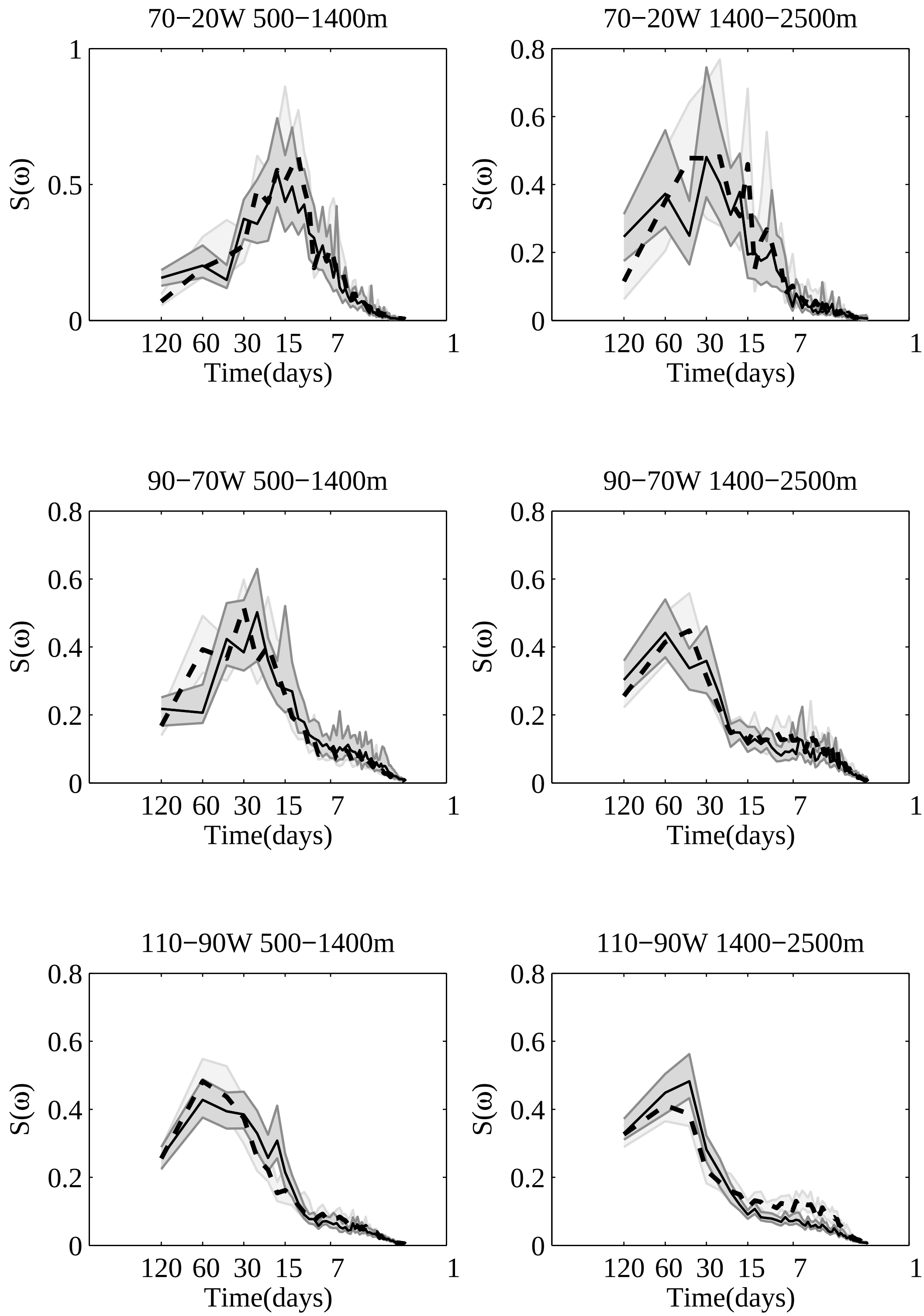

FIG. 14: Variance preserving lagrangian spectra from float velocity. Zonal velocity (solid line with dark shading) and meridional velocity (dashed with light shading). Errorbars are obtained by bootstrapping.

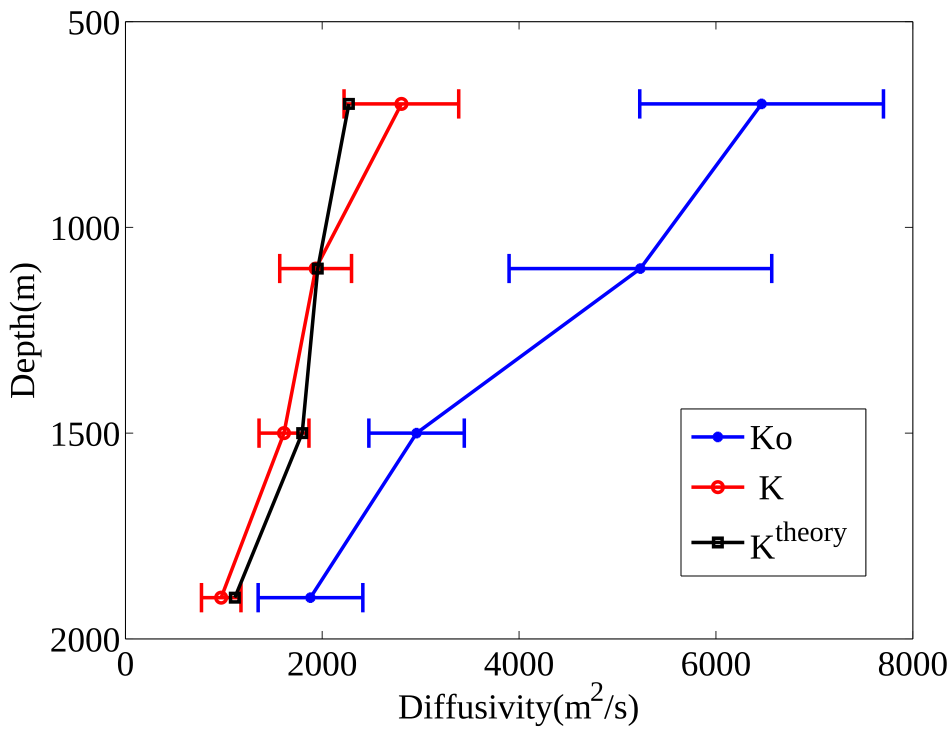

FIG. 15: Vertical structure of meridional diffusivity in the Southeast Pacific Ocean. The diffusivity scale $Ko = EKE.T_{evv}$ (blue) is calculated using only the decay time scale from the floats, the estimated value $K = EKE.T^{l}_{vv}$ (red) is calculated using the full lagrangian time scale from the floats and the value $K^{theory} = \frac{4EKET_{eij}T^{theory2}_{dij}}{\pi^2 T^2_{eij} + 4T^{theory2}_{dij}}$ (black) is calculated using the decay time scale from the floats and meander time scale from theory, which assumed a length scale of 100km.

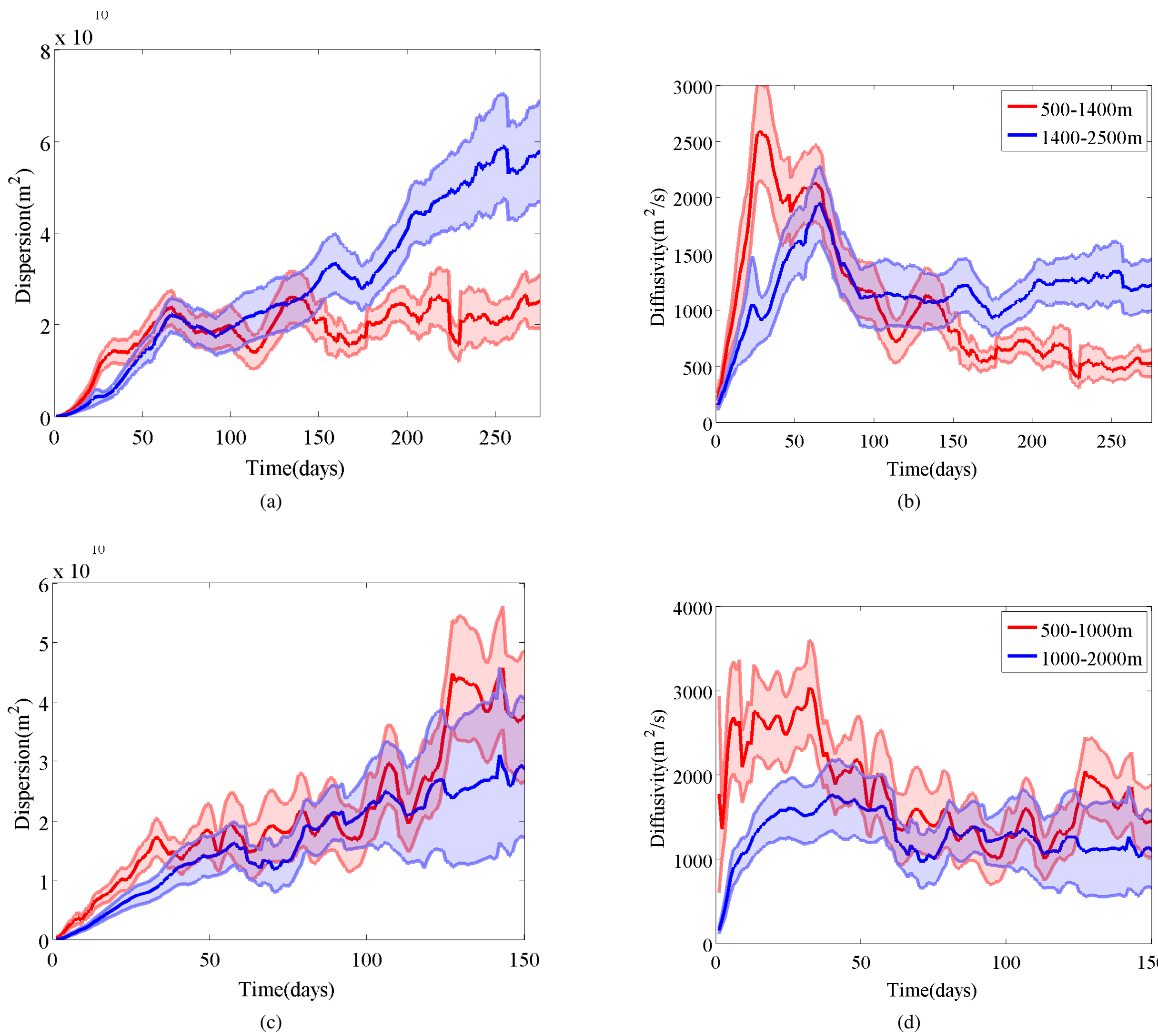

FIG. 16: Dispersion (a) and diffusivity (b) for the floats launched west of 100^oW in the Southeast Pacific Ocean divided into vertical bins encompassing 500-1400m and 1400-2500m. Dispersion (a) and diffusivity (b) for the floats that crossed 70^oW into the Scotia Sea and divided into vertical bins encompassing 500-1000 m and 1000-2500 m.